Available online at www.sciencedirect.com

Chemical Engineering Research and Design

journal homepage: www.elsevier.com/locate/cherd

Effect of temperature and time on the hydrothermal synthesis of WO_3-AgCl photocatalysts regarding photocatalytic activity

Priscila Hasse Palharim[a,*], *Maria Clara D.'Amaro Caira*[a], *Carolina de Araújo Gusmão*[a], *Bruno Ramos*[a,b], *Gabriel Trindade dos Santos*[c], *Orlando Rodrigues Jr.*[d], *Antonio Carlos Silva Costa Teixeira*[a]

[a] *AdOx – Research in Advanced Oxidation Processes, Department of Chemical Engineering, Escola Politécnica, University of São Paulo, 05088000 São Paulo, Brazil*

[b] *Laboratory of Ceramics Processing, Department of Metallurgical and Materials Engineering, Escola Politécnica, University of São Paulo, 05088000 São Paulo, Brazil*

[c] *Programa de Pós-graduação em Ciência dos Materiais - PGCIMAT, Escola de Engenharia, Federal University of Rio Grande do Sul, 90010150 Rio Grande do Sul, Brazil*

[d] *Nuclear and Energy Research Institute, 05508000 São Paulo, Brazil*

ARTICLE INFO

Article history:
Received 31 May 2022
Received in revised form 6 October 2022
Accepted 27 October 2022
Available online 31 October 2022

Keywords:
Composite materials
Heterojunction
Photodegradation
Acetaminophen
Simulated sunlight

ABSTRACT

Heterogeneous photocatalysis is an important and promising alternative for efficient water and wastewater treatment processes. The synthesis of composite materials has attracted attention due to their improved photocatalytic activity and stability. In the present work, composites made of WO_3-AgCl were synthesized by a simple one-step hydrothermal method. The evaluation of the effects of reaction temperature and synthesis time for this composite is reported for the first time. The materials were characterized by XRD, SEM, TEM, EDS, BET, UV–vis DRS, XPS, EPR and PL. All photocatalysts showed broad-spectrum activity due to their strong absorption in the UV region and some absorption in the visible region. The morphology of the materials was highly influenced by the synthesis temperature and time, which affected the photocatalytic efficiency. All materials exhibited good photocatalytic activity under simulated sunlight, with maximum acetaminophen removal of 99.6% for the catalyst synthesized at 120 °C and 12 h. Stability tests showed considerable stability after four cycles. The main reactive species participating in the photodegradation reaction were found to be $O_2^{\bullet-} > h^+ \sim {}^{\bullet}OH$. The heterojunction formed between AgCl and WO_3 plays an important role in the photocatalytic activity, especially when the AgCl surface is not completely covered by WO_3.

1. Introduction

Pollutants of emerging concern have attracted growing attention because of their limited removal by conventional water treatment processes and potential negative impact on the environmental and human health (Tobajas et al., 2017; Tisa et al., 2014). Several technologies have been used for water treatment, such as coagulation, adsorption, sedimentation, and biological processes (Taoufik et al., 2021; Wang et al., 2021a; Chen et al., 2020); while such approaches are effective for removing particulate solids and organic matter, they have little impact on the removal of numerous emerging pollutants, such as pharmaceuticals, hormones

* Corresponding author.
E-mail addresses: ppalharim@usp.br (P.H. Palharim), acscteix@usp.br (A.C.S.C. Teixeira).

https://doi.org/10.1016/j.cherd.2022.10.045

and pesticides (Mestre and Carvalho, 2019; Ikehata et al., 2006). Acetaminophen (ACT, N-(4-hydroxyphenyl)acetamide), also known as paracetamol, is one of the most popular analgesic and antipyretic drugs in the world (Tobajas et al., 2017) and is one of those emerging pollutants. ACT was found in effluents from pharmaceutical facilities at concentrations ranging from 0.281 to 461 μg L^{-1} in Canada (Kleywegt et al., 2019), while in hospital effluent in Brazil, at a maximum concentration of 5470 μg L^{-1} (Vieira et al., 2021). In addition, high concentrations of 36–500 μg L^{-1} were detected in effluents from effluent treatment plants in Canada (Guerra et al., 2014), and in Brazilian surface water bodies ACT from 0.280 to 13.5 μg L^{-1} was found (Montagner et al., 2019). The presence of ACT in water bodies may negatively affect various aquatic organisms, being bioaccumulated in some organisms and transferred to others. Aquatic toxicity, genotoxicity, resistance development in pathogenic bacteria and endocrine disruption are some of the adverse effects of pharmaceutical pollutants, including ACT (Yang et al., 2008). Considering its potential negative impact on aquatic organisms, a promising alternative in its degradation is the application of advanced oxidative processes, such as heterogeneous photocatalysis (Yang et al., 2008; Peng et al., 2017; Palharim et al., 2022; Gusmão et al., 2022; Fan et al., 2018).

Heterogeneous photocatalysis involves the use of a material, typically a semiconductor, which absorbs photons and promotes the local generation of reactive oxidant species, capable of reacting with organic contaminants to convert them mainly into CO_2, H_2O and inorganic salts. In the photocatalytic process, the pollutant oxidation may result from two simultaneous fundamental mechanisms, being the first the oxidation of adsorbed H_2O molecules by the photogenerated positive holes, and the second, the reduction of electron acceptors, such as dissolved O_2, by photogenerated electrons, which leads to the production of hydroxyl and superoxide radicals (Ge et al., 2019; Pelaez et al., 2012).

Among the semiconductors applied to photocatalytic processes, titanium dioxide is by far the most widely used due to its low cost, non-toxicity and chemical stability. However, TiO_2 has limitations in the absorption of visible light, since its band gap energy (3.2 eV) corresponds to a maximum wavelength absorption of 385 nm, making it poorly effective under visible and natural irradiation. Moreover, TiO_2 also presents a high charge recombination rate, which can considerably impair its photocatalytic activity. Therefore, several studies have been focusing on materials that perform better than TiO_2 in photocatalytic applications (Palharim et al., 2022; Gusmão et al., 2022). In this context, WO_3-based catalysts appear as a potential alternative due to their lower energy band gap (2.5–2.8 eV), high thermal stability, and chemical inertness (Yu et al., 2019a; Farhadian et al., 2015). Another advantage of WO_3 is its ability to absorb about 12 % of the solar spectrum and visible light up to about 470 nm, making it more attractive than TiO_2 for sunlight-driven processes (Zheng et al., 2011; Costa et al., 2018).

In addition, the valence band of WO_3 is about 3.1 eV, making its photogenerated holes strongly oxidizing. However, since its conduction band is about 0.4 eV, the photoelectrons have a weak reduction activity, easily accumulating in the CB and increasing recombination rates (Murillo-Sierra et al., 2021a; Mu et al., 2014). Therefore, the recombination of photogenerated e^-/h^+ pairs in WO_3 is a relevant issue to overcome for its photocatalytic application (Deng et al., 2019). The formation of heterojunctions with WO_3 is an attractive possibility to improve its photocatalytic activity. Among the materials that are currently used in the formation of heterojunctions with WO_3 are g-C_3N_4 (Deng et al., 2019; Zhang et al., 2021), TiO_2 (Keller and Garin, 2003; Liu et al., 2020a; Wang et al., 2021b), ZnO (Zhang et al., 2020), Bi_2MoO_6 (Han et al., 2021), SiC (Li et al., 2021), $BiVO_4$ (Dehdar et al., 2021), ZnS (Murillo-Sierra et al., 2021b), and silver-based materials (Palharim et al., 2022; Yu et al., 2019a; You et al., 2021; Ghattavi and Nezamzadeh-Ejhieh, 2019), i.e., AgCl.

There are several techniques conventionally used to synthesize photocatalysts, such as sol-gel method (Chai et al., 2016), precipitation (Munawara et al., 2004), chemical vapor deposition (Chen et al., 2022), anodization (Zych et al., 2022), and hydrothermal reaction (Adhikari et al., 2013; Bi et al., 2019; Jiao et al., 2011). The synthesis procedure is critical for the control of properties regarding elemental composition, crystalline structure, and surface morphology (Biswas et al., 2012). *Hydrothermal synthesis* is a simple and low-cost approach compared to others. Moreover, it allows a fine control over the morphology, crystallinity and size of the prepared material (Palharim et al., 2022; Biswas et al., 2012). Therefore, investigations involving different synthesis conditions are required to evaluate how these properties may enhance charge separation, with improved photocatalytic efficiency. Previous studies have already been conducted on the effect of pH (Murillo-Sierra et al., 2021a; Biswas et al., 2012), the presence of surfactants (Fang et al., 2016), calcination temperature (Mu et al., 2014; Liu et al., 2020b), the amount of dopant (Yu et al., 2019a; Zheng et al., 2011), and the nature of the acids used in the synthesis (Palharim et al., 2022). Regarding this last study, it was previously concluded that the best material in terms of structure and photocatalytic performance was obtained with HCl at pH 1.5; however, further improvements to the catalysts are needed. In general, these studies are conducted for the preparation of WO_3 alone, i.e., not in combination with other materials.

Some studies have focused on the synthesis of WO_3-AgCl-based materials by the hydrothermal method for application in heterogeneous photocatalysis. Adhikari et al. (2013) used a hydrothermal procedure at 200 °C and for 2 h to synthesize Ag-AgCl-WO_3, and obtained 60 % of rhodamine B removal after 240 min of reaction. Senthil et al. (2019) adopted 160 °C and 12 h as synthesis conditions to obtain WO_3-AgCl, which was able to completely remove rhodamine B after 30 min. Likewise, 180 °C and 24 h were set to synthesize WO_3-AgCl by Yu et al. (2019a), who achieved removal percentages of 98 % for methyl orange and rhodamine B. Other authors used combined methods, such as hydrothermal (180 °C and 12 h) followed by precipitation and photoreduction to synthesize Ag-AgCl-h-WO_3, reaching 99.6 % removal of rhodamine B after 9 min of reaction. It is clear that there is no consensus on the ideal conditions of hydrothermal synthesis for producing WO_3-AgCl-based photocatalysts. Hence, to the best of our knowledge, no previous study has evaluated the effect of reaction time and temperature simultaneously, for the synthesis of WO_3 coupled to AgCl. In the present work, the effect of these parameters on the properties and efficiency of the catalyst, assessed by the extent of degradation of ACT in water under simulated solar radiation, was determined by a deep evaluation of morphological, optical, and crystalline properties, obtained from several characterization techniques.

2. Materials and methods

2.1. Materials

Acetaminophen ($C_8H_9NO_2$, HPLC standard, ≥ 99%), sodium tungstate dihydrate ($Na_2WO_4{\cdot}2H_2O$, ACS, ≥ 99 %) , silver nitrate ($AgNO_3$, ACS, PA) and 5,5-dimethyl-1-pyrroline N-oxide (DMPO) were purchased from Sigma-Aldrich. Concentrated hydrochloric acid (36–38 % HCl) and ethanol were of analytical grade. Deionized Milli-Q® water (18.2 MΩ) was used as solvent in all steps of the investigation.

2.2. Synthesis of photocatalysts

All photocatalysts were synthesized via the one-step hydrothermal method (Palharim et al., 2022). Briefly, a proportional amount of $AgNO_3$ was added to 15 mL of an aqueous solution of 0.3-mol L^{-1} $Na_2WO_4{\cdot}2H_2O$ to achieve WO_3-5% Ag (w/w). This solution was continuously stirred for 30 min before the pH was adjusted to 1.5 using HCl, and kept under magnetic stirring for another 30 min. The final solution was transferred to a 220-mL PTFE-lined autoclave, which was transferred to a laboratory oven and heated to 120 or 180 °C at 10 °C min^{-1}. The solution was then allowed to age in the autoclave for 6, 12, 24 or 48 h, producing a total of eight materials. To eliminate any possible ionic residues, the solid obtained was re-suspended and washed three times with ethanol and once with water. The final dispersion was dried for 24 h at 80 °C, and the resulting solid was finely ground with mortar and pestle before storage and use.

2.3. Photocatalysts characterization

Scanning electron microscopy (SEM) and transmission electron microscopy (TEM) were used to examine the morphology of the produced materials. A sample suspension in isopropanol was dripped on a silicon substrate and dried for SEM analyses, which were conducted in a SEM (Vega 3 LMU Tescan equipment) at 5 and 20 kV. The suspension was dripped over a carbon-coated copper grid for TEM analysis, and a JEM-2100 (Jeol) microscope running at 200 kV was employed. Energy dispersive X-ray spectroscopy (EDS) was used to map the elemental composition of the catalysts (Oxford equipment coupled to SEM). X-ray powder diffraction (XRD) patterns were achieved using a D8 Focus Bruker AXS system with a Cu K-radiation source and Ni filter at 20 kV and 40 mA. XPS analysis was used to examine the element surface composition and the chemical states of the materials, measured on a K-Alpha Thermo Scientific photoelectron spectrometer with a X-ray source (Al K_α) and pressure of 1×10^{-8} mBar. UV–vis diffuse reflectance spectra (UV–vis DRS) were recorded using a Shimadzu 2550 spectrophotometer with an integrating sphere. BET surface areas were measured by N_2 adsorption using a Gemini III 2375 equipment (Micromeritics Instrument Corp.). Photoluminescence spectroscopy (PL) was evaluated at room temperature using a Horiba Yvon-Jobin Fluoromax-222 (Em/Exc; slit 1.0 nm) at the 350–700 nm region equipped with a xenon lamp and a peltier-cooled FL-123450 PMT detector. Finally, the material that showed the best photocatalytic activity was analyzed by electron paramagnetic resonance spectroscopy (EPR) using a Bruker EMXplus operating in X-band at room temperature.

2.4. Photocatalytic activity assays

Acetaminophen (ACT) was used as a model contaminant to evaluate the photocatalytic activity of the synthesized photocatalysts. 10 mg of the catalyst was dispersed into 10 mL of 5-mg L^{-1} ACT solution, in a 25-mL beaker. A thermal bath was used to keep the reaction temperature at 21 °C. To achieve adsorption–desorption equilibrium, the suspension was stirred in the dark for 30 min. Subsequently, the experiments were conducted for 120 min using a high-power metal halide lamp (400 W HPI-T, Phillips Co.) placed at 15 cm from the solution surface. The lamp is assembled on a parabolic reflector equipped with a 1.5-mm flint glass protection. A spectroradiometer (Luzchem, SPR-4002) was used to measure the irradiance on the solution surface, of 4.6 mW cm^{-2}. 200-µL samples were collected over time, diluted five times, filtered and analyzed by HPLC. An HPLC Shimadzu LC20 chromatograph, equipped with a C18 column (Prominent) and with a UV–vis detector (SPD20A) was used to quantify the ACT concentration. Methanol:water (25:75) was used as the mobile phase, at a flow rate of 1.0 mL min^{-1}, injection volume of 50 µL and oven temperature of 35 °C. The detection wavelength and the retention time were 243 nm and 7 min, respectively. The limit of ACT detection was 0.08 mg L^{-1} and the limit of quantification was 0.24 mg L^{-1}.

3. Results and discussion

3.1. Phase structure

The XRD diffractograms shown in Fig. 1a have well-defined peaks, indicating that the prepared catalysts exhibit high crystallinity and are free of impurities. The patterns were found to match well with the JCPDS Cards No. 00–033–1387 of the WO_3 hexagonal structure and No. 96–901–1667 of the cubic phase of AgCl. An extra peak at 16.3° was found in the sample synthesized at 120 °C for 12 h, referring to the crystal plane (020) of the JCPDS Card No. 96–150–9985 of the $W_8Ag_{16}O_{32}$ orthorhombic structure. The peaks of cubic metallic Ag crystals could not be clearly identified, possibly due to the low concentration of silver in all samples.

The peaks at 32.3° and 46.2° associated with the crystal planes (002) and (022), respectively, of AgCl are more evident in the samples synthesized at 120 °C, revealing that this temperature favors the growth of AgCl crystals. In the samples WO_3-AgCl (120–6) and WO_3-AgCl (120–12), these peaks appear with higher intensities, implying that the reaction times of 6 and 12 h are optimal for the synthesis of AgCl. Additionally, an extra peak at 27.8°, partially overlapping the (200) crystal plane of WO_3, is particularly observed in the samples synthesized at 120 °C. This peak corresponds to the (111) crystal plane of AgCl, and once again indicates that AgCl particles growth is preferred at the lower synthesis temperature. Although the two peaks overlap, the first plane is observed to have higher intensity than the second only for the WO3-AgCl (120–12) catalyst. Furthermore, the XRD pattern of the bare WO_3, synthesized at 120 °C and for 12 h, is depicted in Fig. S1, which corresponds to the JCPDS Card No. 00–033–1387 of the WO_3 hexagonal structure, as seen in the composite materials.

The crystal lattice parameters, calculated by the Rietveld method (Sujiono et al., 2021), and the crystallite sizes of WO_3 and AgCl, obtained by the Scherrer equation, are shown in Table 1. The calculated lattice parameters show values very

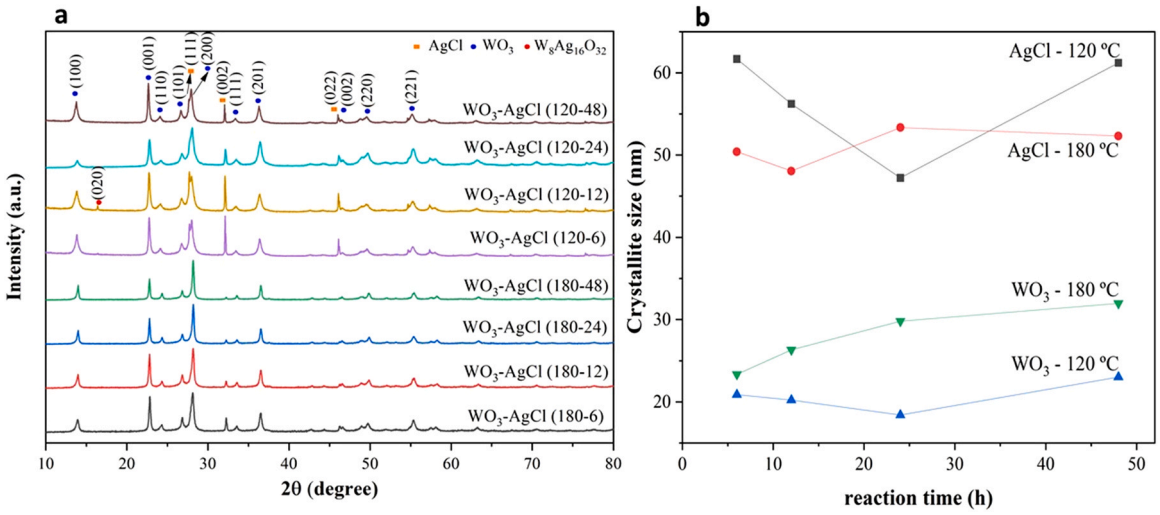

Fig. 1 – (a) XRD patterns and (b) variation in crystallite size for the photocatalysts synthesized at different reaction temperatures and times.

similar to those from the JCPDS Card No. 00–033–1387 of WO_3 (a = b = 7.30 Å and c = 3.90 Å). The slight difference from the standards is expected, and can be understood as an effect of the coupling between AgCl and WO_3. In addition, neither the synthesis temperature, nor its duration resulted in appreciable changes in the lattice parameters. The Williamson-Hall plot was used to estimate the microstrain for each material. Nevertheless, the obtained data showed a poor linear fitting, with dispersed scatters, which is related to the anisotropy in the strain broadening component; and, therefore, does not allow the microstrain estimation (Irfan et al., 2018).

The variation of crystallite sizes for all synthesized materials is depicted in Fig. 1b, clearly showing that AgCl has grown larger than WO_3. In general, the size of WO_3 crystallites increased with increasing temperature, keeping the synthesis time. This is expected because the nucleation and growth rate of the particles increase as temperature is boosted (Wasly et al., 2018), as well as because of nanocrystal coalescence (Collazzo et al., 2011). Conversely, in general, the crystallite sizes of AgCl decreased as temperature increased. Furthermore, at 120 °C, the size of AgCl crystallites decreased until reaching minimum values in 24 h of hydrothermal reaction, increasing again. A similar behavior was observed at 180 °C, but the minimum crystallite size was obtained within 12 h of reaction, subsequently increasing and remaining nearly constant afterwards. As already observed from the XRD patterns, AgCl growth is not favored at 180 °C; thus, the prevailing growth of WO_3 at this temperature could have inhibited the growth of AgCl, thus resulting in smaller AgCl crystallites at higher temperatures, for the same reaction time.

According to Table 1 and Fig. 1b, it is observed for the materials synthesized at 120 °C: (i) although the crystallite size of WO_3 is nearly the same for all reaction times studied, it slightly decreases until reaching 24 h of synthesis and then increases, achieving the maximum value of 23.0 nm; (ii) the crystallite size of AgCl decreases as the reaction time is prolonged, reaching a minimum size of 47.2 nm at 24 h of synthesis and then increases to 61.2 nm at 48 h of reaction. A possible explanation for this decrease in AgCl crystallite size could be the growth of other crystals around these crystallites.

For the photocatalysts synthesized at 180 °C, it can be said: (i) the crystallite size of WO_3 increased with synthesis time; (ii) there is no clear pattern in the crystallite size of AgCl in relation to the different synthesis times studied here. The increase in crystallite size according to the time of synthesis is generally observed, as longer reaction times favor a greater coalescence of the particles (Collazzo et al., 2011).

3.2. *Morphology*

Fig. 2 exhibits the SEM images of the photocatalysts synthesized at 120 °C at different times of reaction. Rectangular

Table 1 – Lattice parameters, crystal size, N_2-BET surface areas, band gap energies and absorption edges of the synthesized materials.

Sample*	Lattice parameters (Å)		Crystallite size (nm)		Surface area ($m^2\ g^{-1}$)	E_g (eV)	λ (nm)
	a = b	c	WO_3	AgCl			
WO_3-AgCl (120–6)	7.39	3.88	20.9	61.7	18.79	2.89	429
WO_3-AgCl (120–12)	7.40	3.91	20.2	56.2	29.51	2.87	432
WO_3-AgCl (120–24)	7.36	3.90	18.4	47.2	38.61	2.82	439
WO_3-AgCl (120–48)	7.43	3.92	23.0	61.2	26.04	2.87	432
WO_3-AgCl (180–6)	7.35	3.89	23.4	50.4	15.35	2.90	428
WO_3-AgCl (180–12)	7.35	3.90	26.3	48.1	23.01	2.89	429
WO_3-AgCl (180–24)	7.32	3.90	29.8	53.3	27.18	2.84	437
WO_3-AgCl (180–48)	7.32	3.90	32.0	52.3	16.29	2.91	426

*The first number in parentheses represents the synthesis temperature (°C) and the second number represents the synthesis time (h).

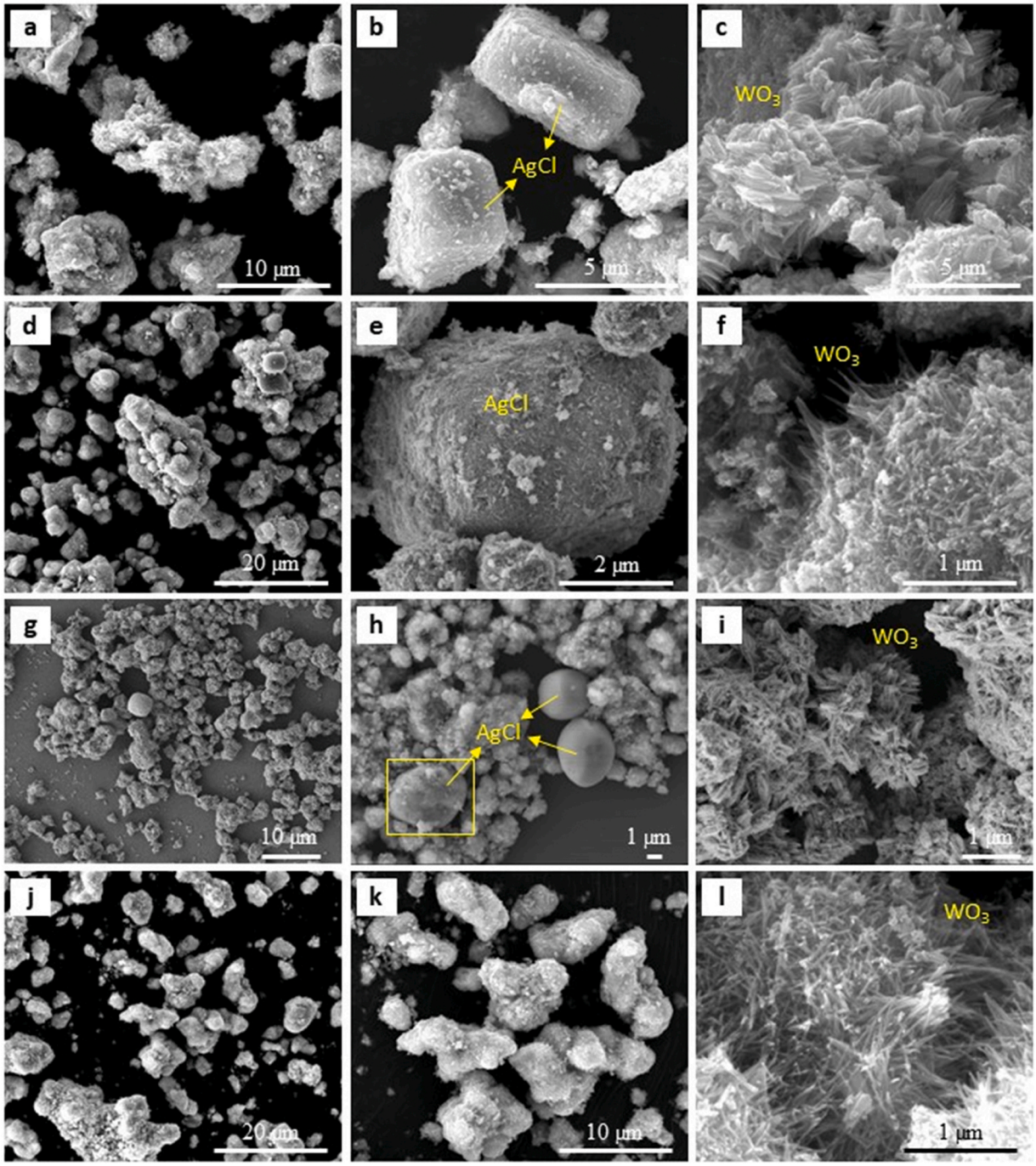

Fig. 2 – SEM images of WO_3-AgCl photocatalysts synthetized by hydrothermal method at 120 °C for (a-c) 6 h, (d-f) 12 h, (g-i) 24 h and (j-l) 48 h of reaction time.

prisms with equivalent length of ~5.2 μm are observed for the sample synthesized in 6 h (Fig. 2b), which are addressed to AgCl particles. WO_3 particles can be seen adhered to the AgCl particles (Fig. 2b), as a mixture of agglomerated sharp layers (Fig. 2c). AgCl and WO_3 particles were confirmed by EDS analysis, as shown in Fig. S2, where Cl and Ag were detected in the rectangular prisms with high intensity peaks; while W, O were identified in the rest of the material, suggesting that these regions refer to the WO_3 particles. The AgCl and WO_3 particles were confirmed by EDS analysis, according to Fig. S2, where Cl and Ag peaks were detected with great intensity in the rectangular prisms; while W, O and Ag peaks were identified in the rest of the material, showing that WO_3 is probably decorated with silver particles. By increasing the synthesis time to 12 h (Fig. 2e), the rectangular prisms had their shape changed to cube-like or quasi-spherical, with average size of 3.9 μm. On the other hand, the WO_3 particles started becoming more well-defined, with a shape similar to an agglomerate of thin sticks (Fig. 2f). At the same time, more WO_3 particles can be seen on the surface of AgCl (Fig. 2e). A further increase in the reaction time to 24 h led to the formation of quasi-spherical AgCl particles with average size of 4.2 μm (Fig. 2h). Some AgCl particles were almost completely covered by the WO_3, as observed in the yellow square indicated in Fig. 2h. Meanwhile, the WO_3 continued growing and thicker rods were

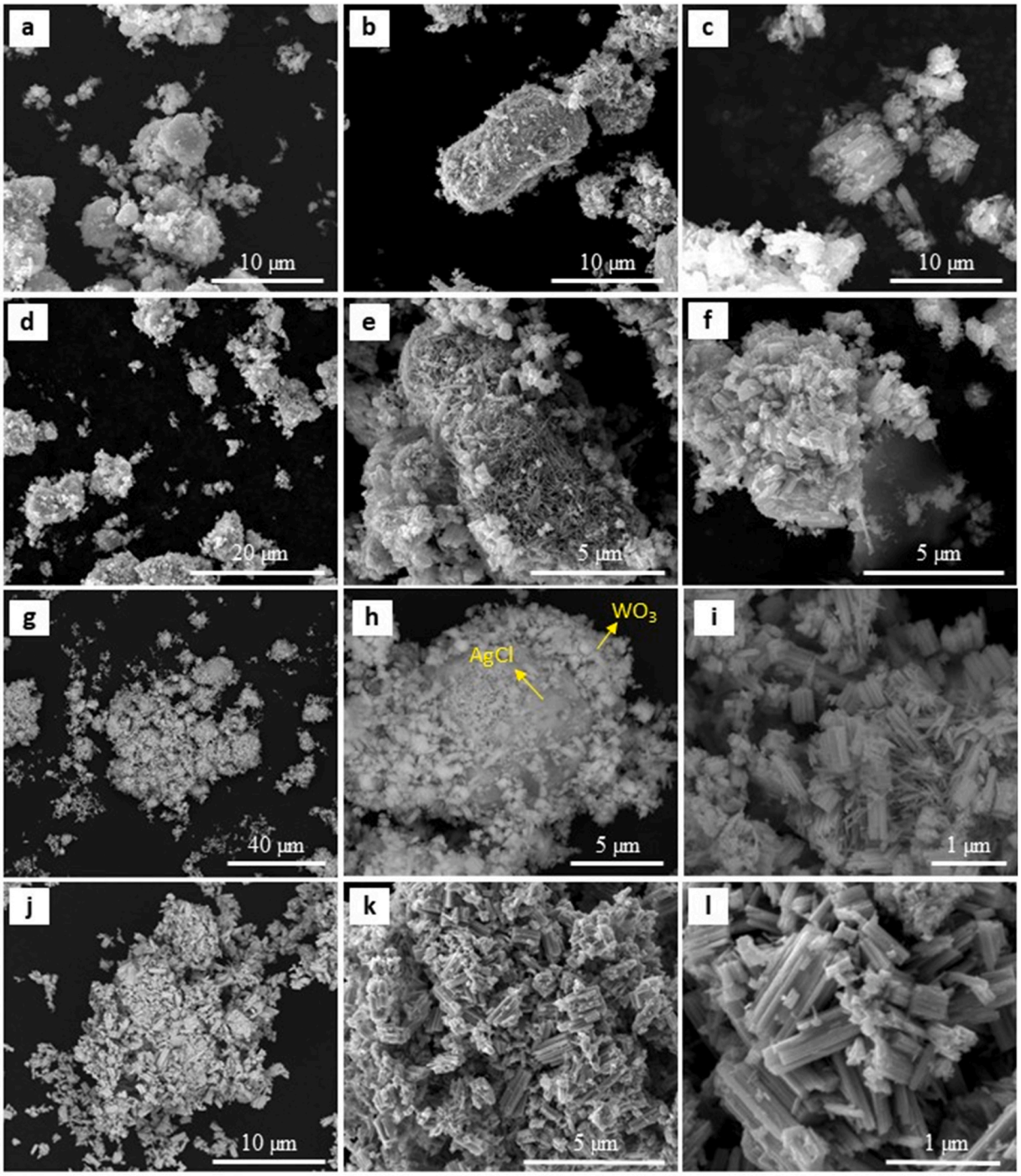

Fig. 3 – SEM images of WO_3-AgCl photocatalysts synthetized by the hydrothermal method at 180 °C for (a-c) 6 h, (d-f) 12 h, (g-i) 24 h and (j-l) 48 h of reaction time.

detected (Fig. 2i). As the reaction time extended to 48 h, the AgCl particles kept the quasi-spherical-like shape, but were completely covered by WO_3 particles (Fig. 2k), which grew disorderly as thicker rods (Fig. 2l).

From Fig. 3a-b, which show the SEM images of the photocatalysts synthesized at 180 °C and 6 h, particles of up to ~12 μm can be seen completely covered with smaller particles of rectangular prisms to nanorods shape. When the reaction temperature increases to 12 h, the WO_3 particles had a morphology of rectangular prisms and nanorods of different sizes, both with more definition compared to the material synthesized at 6 h (Fig. 4e-f). An additional increase in reaction time to 24 h led to a decrease in the number of nanorod-like particles and an increase in the number of the agglomerated rectangular prisms (Fig. 3i). Interestingly, this was the only material synthesized at 180 °C in which AgCl particles could be seen by SEM, despite being almost completely covered by WO_3 (Fig. 3 h). The EDS spectra of the materials synthesized at 180 °C for 6, 12 and 24 h are shown in Fig. S3. Finally, after 48 h of reaction, the WO_3 agglomerated in rectangular prisms in a disoriented way became dominant in the sample (Fig. 3l). Except for the sample synthesized at 180 °C and 24 h, the other materials produced at 180 °C did not exhibit any AgCl particles by SEM images, as was seen in the samples prepared at 120 °C. Nevertheless, although chlorine was not detected in the EDS analyses (Fig. S3a-b),

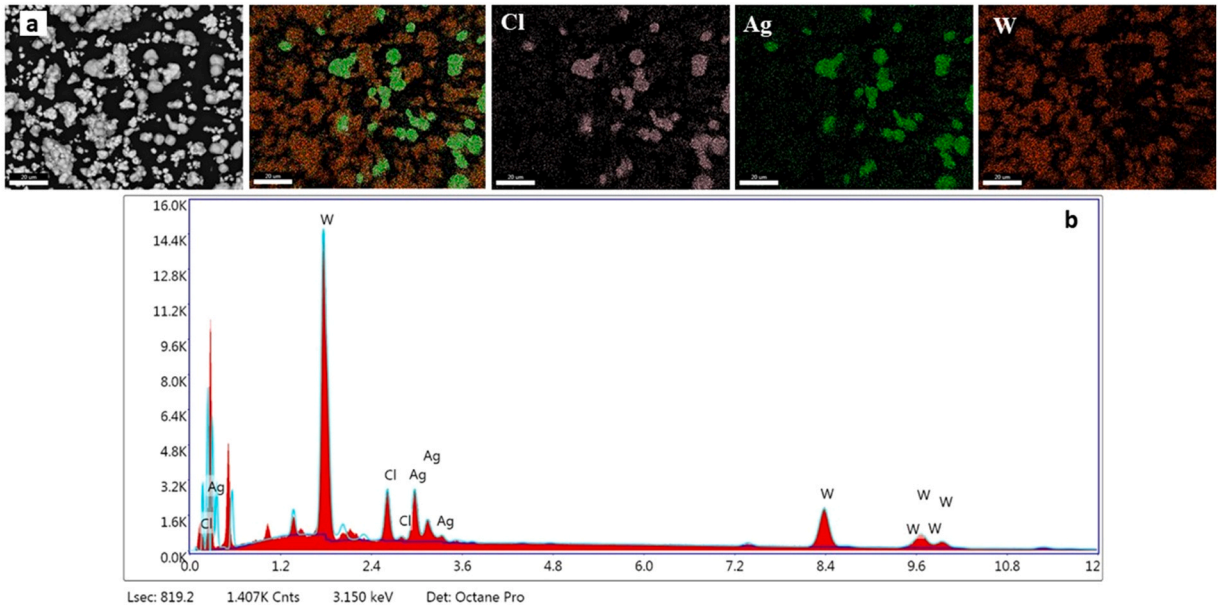

Fig. 4 – (a) Energy dispersive spectroscopy elemental mapping image and (b) energy dispersive X-ray spectra (EDS) of the WO_3-AgCl photocatalyst synthesized at 120 °C and 12 h.

AgCl is believed to be present in the sample under the WO_3 particles, which grew adhered to it. In fact, XRD analysis exhibited AgCl peaks for all catalysts, but less intense for the 180 °C-samples, confirming the presence of AgCl particles.

The WO_3-AgCl (120–12) photocatalyst was further analyzed by elemental mapping and energy dispersive spectrometry. Fig. 4 indicates the presence of W, Ag and Cl in the sample, with no impurity peaks. In the scanned region, the material contains 48.8 % W, 20.0 % Ag and 31.2 % Cl (atomic percentage). Tungsten is evenly distributed throughout the sample, while Cl and Ag are detected at specific locations, once again confirming the formation of AgCl, as already observed in our previous work (Palharim et al., 2022). Thus, the material synthesized at 120 °C and 12 h is not morphologically homogeneous, but composed of rectangular prisms to quasi-spherical AgCl and rod-shaped particles of WO_3 (Figs. 2 and 4).

The WO_3-AgCl (120–12) photocatalyst was also analyzed by TEM, TEM-EDS and HRTEM. Fig. 5a-b depict the mixed morphology of the catalyst, which is composed of nanorods ranging in length from 27.3 to 70.9 nm, and some quasi-spherical particles. Fig. 5c reveals that the quasi-spherical particles can be AgCl, while the nanorods are addressed to WO_3 particles. It is worth noting that the AgCl particles observed by TEM (Fig. 5) are different from those detected by SEM (Fig. 2e), since the latter are micrometric in size and the former are mostly nanometric. Therefore, it can be said that the WO_3-AgCl (120–12) photocatalyst is composed of WO_3 nanorods and micro and nanometric quasi-spherical AgCl.

Some selected areas were analyzed by HRTEM, which confirmed the high crystallinity of the material by the clear lattice boundary (Fig. 5d). From Fig. 5d, lattice spacings of 3.91 Å and 1.96 Å can be identified, corresponding to the (001) crystalline plane of hexagonal WO_3 (JCPDS Card No. 00–033–1387) and to the (022) plane of the cubic phase of AgCl (JCPDS Card No. 96–901–1667), respectively, indicating the formation of a complex composite.

Finally, the selected area electron diffraction (SAED) (Fig. 5e) exhibits concentric circles, confirming the polycrystallinity of the structure. Six crystalline planes of hexagonal WO_3 were detected by SAED pattern, including (010), (110), (020), (111), (021), (122); and the (022) plane of AgCl. The results from HRTEM and SAED corroborate those obtained by the XRD patterns, and suggest the formation of a heterojunction between WO_3 and AgCl.

3.3. *Chemical states*

The chemical states and elemental composition of the WO_3-AgCl (120–12) photocatalyst were evaluated through XPS analysis, as shown in Fig. 6. All data were adjusted to the position of C 1s, i.e., 284.8 eV; the CasaXPS software was used for data fitting. The typical survey scan XPS spectrum (Fig. 6a) reveals that the photocatalyst contains mainly W, O, Ag, Cl. The element carbon observed in the spectrum is from the XPS instrument and sodium is from the sodium tungstate precursor used in the catalyst synthesis. The high-resolution XPS spectra of W 4f, O 1s, Ag 3d and Cl 2p were conducted in order to identify the chemical states of the elements. Four peaks could be fitted to the two W 4f peaks (Fig. 6b): two strong peaks at 35.27 and 37.44 eV, corresponding to W $4f_{7/2}$ and W $4f_{5/2}$ of W^{6+}; and two smaller peaks at 35.45 and 36.58 eV, corresponding to W $4f_{7/2}$ and W $4f_{5/2}$ of W^{5+} (Chai et al., 2019; Wang et al., 2018). Thus, the surface of the photocatalyst contains two valence states of tungsten (Chai et al., 2019), with oxygen vacancies (Li et al., 2019).

For O 1s (Fig. 6c), three peaks were observed at 529.82, 530.89 and 533.17 eV, assigned to the lattice oxygen of O-W bond, to adsorbed O_2, and to OH^- groups (from the absorbed water), respectively (Chai et al., 2019). The two Ag 3d peaks (Fig. 6d) were divided into two peaks at 366.25 and 372.19 eV belonging to Ag $3d_{5/2}$ and Ag $3d_{3/2}$ of Ag^+ (Senthil et al., 2019), and two peaks at 367.71 and 374.58 eV attributed to Ag $3d_{5/2}$ and Ag $3d_{3/2}$ of Ag^0 (Fang et al., 2019), respectively. Although the slight shoulder identified in the Ag 3d peaks correspond to the Ag^0, it was not possible to identify Ag by XRD or TEM analyses. Thus, it is difficult to affirm that the synthesized sample contains Ag^0. In Fig. 6e, two peaks of Cl 2p at 198.43 and 201.49 eV were assigned to Cl $2p_{3/2}$ and Cl $2p_{3/2}$ of Cl^- (Chai et al., 2019).

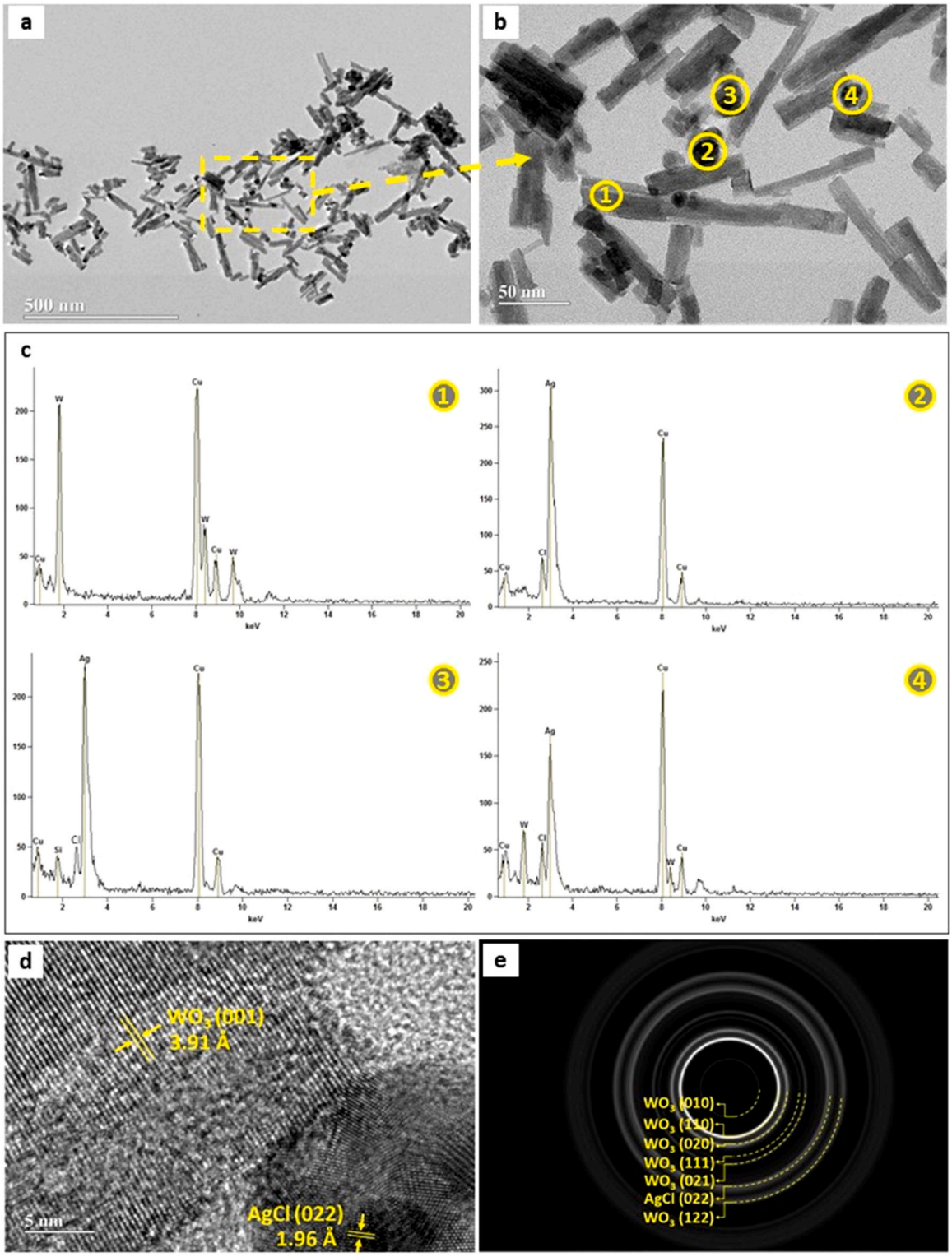

Fig. 5 – (a, b) TEM imagens; (c) EDS spectra; (d) HRTEM image; and (e) SAED pattern of the WO_3-AgCl photocatalyst synthesized at 120 °C and 12 h.

3.4. *Formation mechanism*

As seen from the results above, the morphology of WO_3 and AgCl is highly influenced by temperature and time of synthesis. During the first stage of the synthesis process, i.e., the mixing of precursors, two main reactions occur at the same time: (i) HCl reacts with sodium tungstate forming $H_2WO_4{\cdot}2H0.2H_2O$ (Eq. 1); (ii) HCl reacts with silver nitrate producing AgCl crystals (Eq. 2), which settle immediately. The nucleation process of AgCl particles and their growth start before heating and, according to Guo et al. (2017)., lead to irregularly shaped particles at this point. In turn, the nucleation process of WO_3 starts at temperatures above 60 °C, because it overcomes the decomposition temperature of H_2WO_4 (Park et al., 2017) (Eq. 3). Hassani et al. (2011). concluded that the nucleation step of WO_3 particles occurs before the first hour of hydrothermal reaction and then the formation mechanism is led by the growth process. Wang et al. (2019), who synthesized bare WO_3 by the hydrothermal method, noticed a phase change before 2 h of reaction, from

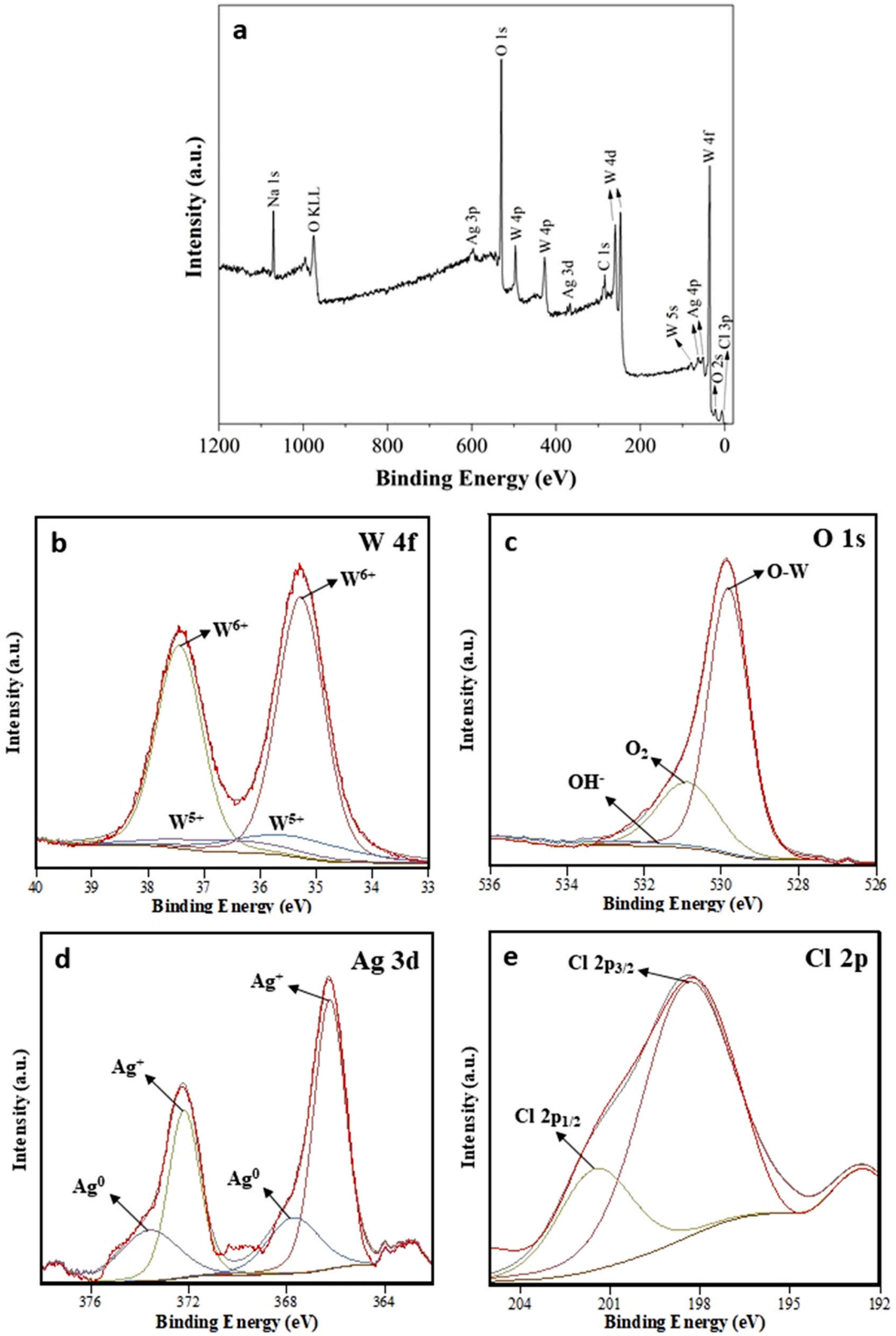

Fig. 6 – XPS spectra of the WO_3-AgCl photocatalyst synthesized at 120 °C and 12 h: (a) survey, (b) W 4 f, (c) O 1 s, (d) Ag 3d and (e) Cl 2p.

orthorhombic to monoclinic; and remarked that at increased synthesis times, the growth process prevailed. Nevertheless, as the XRD patterns (Fig. 1a) revealed similar peaks for all catalysts, no phase transformation was observed in our materials. It is worth noting that we synthesized photocatalysts starting at 6 h of reaction, and it is likely that any phase transformation would have occurred before that. Fig. 7 summarizes the formation mechanism, at different conditions, for the materials synthesized in this work.

$$Na_2WO_4{\cdot}2H_2O + HCl \rightarrow H_2WO_4{\cdot}2H_2O + 2NaCl \quad (1)$$

$$AgNO_3 + HCl \rightarrow AgCl \downarrow + HNO_3 \quad (2)$$

$$H_2WO_4{\cdot}2H_2O \xrightarrow{\Delta} WO_3\,(crystal\ nuclei) + 3H_2O \quad (3)$$

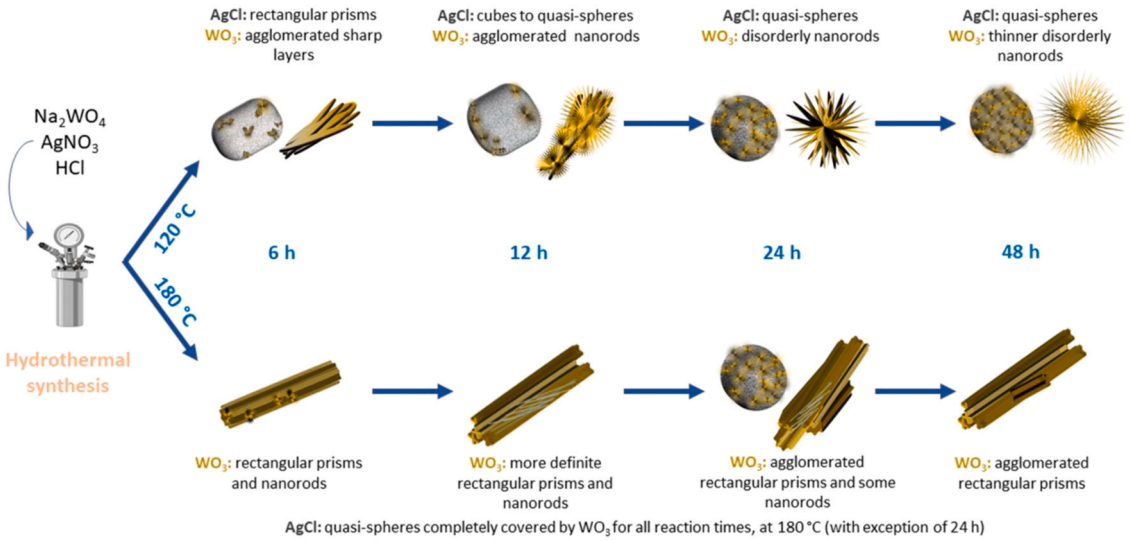

Fig. 7 – Proposed formation mechanism of WO_3 and AgCl particles at different temperatures and times of reaction.

As the present work focuses on the one-spot synthesis of WO_3 and AgCl, the growth mechanism can be said to be different for both materials, depending on the reaction temperature and time. At 120 °C and up to 24 h of reaction time, the growth of AgCl particles prevailed over that of the WO_3 particles, suggesting that the growth rate is higher for AgCl at lower temperature and shorter times. After 6 h of reaction, AgCl were produced as rectangular prisms, and then had their shape changed to quasi-spherical after 24 h. As reaction time increased, some WO_3 particles became more and more adhered to the AgCl surface, almost completely covering it after 24 h, which may have inhibited the continued growth of AgCl. This observation suggests that after 24 h of synthesis, AgCl particles have their growth rate reduced and probably the WO_3 growth rate turns faster.

The slow polar growth that controls the 1D growth of WO_3 nanorods explains the change in WO_3 particles shape from a mixture of agglomerated sharp layers to nanorods as the hydrothermal reaction proceeds. The polar crystals tend to grow at low growth rates along the polar direction (c-axes), especially at low reaction temperatures (Wang et al., 2008). The crystal planes that have higher surface energy will grow at higher velocity (Tong et al., 2006). In this work, the (001) plane is the growth plane of WO_3 particles, as confirmed by the HRTEM analysis (Fig. 5d). As the reaction time proceeds, the smaller nanorods dissolve, promoting the growth of larger nanorods. This process can be explained by the Ostwald ripening mechanism, whereby smaller particles redissolve, allowing the growth of larger ones, due to the high solubility and surface energy of the smaller particles (Thanh et al., 2014). Furthermore, it is suggested that the mixture of agglomerated sharp layers obtained after 6 h may be produced during the cooling and washing processes. Hassani et al. (2011) claimed that the single nanorods generated in the subsequent hours could not be obtained if the mixture of agglomerated sharp layers had been bounded chemically. Thus, the authors suggest that the formation of nanorods is evidence for the late formation of agglomerated sharp layers after hydrothermal synthesis; and that each single crystal of WO_3 would grow from the nuclei at different rates.

For the materials synthesized at 180 °C, in contrast, it was not possible to observe the growth of AgCl particles. As already mentioned, the WO_3 particles may have grown on the AgCl surface during all times of reaction studied in this work, covering it completely. Thus, it can be implied that at 180 °C, the growth rate of WO_3 is higher than that of AgCl. Similarly to the materials synthesized at 120 °C, the Ostwald ripening mechanism seems to drive the growth of the particles. Additionally, particles of different sizes could be detected (Fig. 3l) even after 48 h of reaction, confirming that the nucleation step lasted as long as the growth process. Since the process parameters (temperature and pressure) do not change during the whole synthesis, it can be proposed that the W^{+6} ions leave the solution to form the WO_3 solid phase, leading to a constant or decreased rate of reaction. Therefore, as the nanorods grow larger, their growth rate slows down because they need less W^{+6} ions to turn into WO_3 (Hassani et al., 2011).

3.5. *BET surface area*

Table 1 summarizes the N_2-BET specific surface areas of the WO_3-AgCl materials synthesized at 120 and 180 °C, at different reaction times. In general, the photocatalysts prepared at 120 °C exhibited higher surface areas, which may be due to the material morphology. At 120 °C, the catalysts were composed of rectangular prisms to quasi-spherical AgCl particles, and WO_3 nanorods that became thinner with increasing reaction time; while at 180 °C, the materials consisted of a mixture of agglomerated quasi-spherical AgCl completely covered with assembled WO_3 nanorods. Thus, the high agglomeration of particles observed in the materials synthesized at 180 °C can result in lower values of surface area.

For both synthesis temperatures, the surface area increased until 24 h of reaction and then decreased. The largest surface areas were achieved at 24 h of synthesis for both temperatures (38.61 $m^2\ g^{-1}$ at 120 °C and 27.18 $m^2\ g^{-1}$ at 180 °C), and may be related to the optimum combination of the morphologies of both WO_3 and AgCl particles. In fact, the photocatalyst WO_3-AgCl (120–24), which exhibited the largest BET surface areas, has a combination of quasi-spherical AgCl particles with thin WO_3 nanorods, once again demonstrating that the morphology is directly related to the surface area. The lower surface areas achieved may be associated with the pore structure of the particles (Adhikari et al., 2013).

3.6. Optical properties

The optical properties of the synthesized materials were evaluated through UV–vis diffuse absorbance spectra (DRS), as shown in Fig. S2. All photocatalysts exhibited broad-spectrum activity due to their strong absorption in the UV region and some absorption in the visible region. Moreover, the band gap energy was estimated by the Tauc plot (Table 1), as described by Makuła et al. (2018). It is worth mentioning that modifications introduced in composite materials, such as those synthesized in the present work, can lead to intra-band gap states, which will reflect in the absorption spectrum as an additional broad absorption band, and thus change the Tauc plot. Therefore, it should be taken into consideration to estimate the band gap energy (Makuła et al., 2018).

According to Table 1, the band gap energies of the synthesized materials varied from 2.82 to 2.91 eV, showing that their photocatalytic activity may be intensified under sunlight, when compared to commercial TiO_2 (3.0–3.2 eV) (Adhikari and Sarkar, 2014; Yu et al., 2019a). Generally, there is neither significant difference in the E_g values for the temperatures and times of synthesis studied, nor a clear pattern.

3.7. Photocatalytic activity

The photocatalytic activity of the WO_3-AgCl catalysts synthesized at different temperatures and reaction times was evaluated in the degradation of acetaminophen under simulated sunlight. No significant ACT removal was observed during the 120-min experiments conducted under dark conditions (Fig. S5). From Fig. 8, it can be seen that the photocatalysts synthesized at 120 °C clearly exhibited higher photocatalytic activity compared to those synthesized at 180 °C. For the latter (Fig. 8b), ACT removal increased with increasing reaction time, reaching a maximum removal of 70.5 % after 120 min, for the material synthesized for 24 h; and then, ACT removal decreased to only 54.3 % for WO_3-AgCl (180–48).

Interestingly, the WO_3-AgCl (180–24) sample, which showed maximum removal among the catalysts synthesized at 180 °C, was the only one that allowed the observation of AgCl particles not completely covered by WO_3 in the SEM images (Fig. 3h). From this, it can be suggested that the presence of AgCl particles may have an important role in ACT removal. All the photodegradation data followed a kinetic behavior consistent with a pseudo first-order model, as presented in Table 2. Although the removal efficiency varied according to the reaction time, the rate constants of the materials prepared at 180 °C were all in the same order of magnitude (from 0.011 to 0.017 min^{-1}).

In turn, the photocatalyst synthesized at 120 °C for 12 h showed the highest ACT removal efficiency overall, achieving near complete removal, followed by the 6-h reaction catalyst. The photodegradation run with the WO_3-AgCl (120–12) material showed a rate constant of 0.063 min^{-1}, which is approximately six times higher than the k of the materials produced at 180 °C. The materials synthesized at 24 and 48 h presented good removal efficiencies, but significantly smaller than those exhibited by materials prepared in shorter reaction times. According to the SEM images (Fig. 2a-f), the catalysts with maximum removal efficiencies, i.e., WO_3-AgCl (120–6) and WO_3-AgCl (120–12), exhibited both AgCl and WO_3 particles, with morphologically defined AgCl particles partially covered by the latter. Conversely, when the synthesis time was increased to 24 h, the ACT removal efficiency dropped to 75.6 %; in this case, SEM images (Figs. 2g-1) revealed that some of the AgCl particles were completely covered by WO_3, as well defined nanorods. Thus, this morphology may have negatively influenced the photocatalytic performance of the material. However, with further increase in the synthesis time to 48 h, the WO_3 particles became thicker and disordered, and the ACT removal efficiency increased to 83.6 %. A possible explanation for this increase in removal efficiency could be that, although the AgCl was completely covered, the thicker WO_3 nanorods produced in 48 h could positively enhance the photocatalytic efficiency, compared to the nanorods still in the growth phase.

The photocatalytic efficiency of the materials synthesized in this work can be concluded to indeed be influenced by their morphology, which is deeply affected by the temperature and duration of the synthesis reaction. The establishment of a heterojunction between AgCl and WO_3 plays an important role in photocatalytic activity, especially when the AgCl surface is not completely covered by WO_3 particles.

The stability of the WO_3-AgCl (120–12) photocatalyst was assessed through reuse tests for 120 min, as described elsewhere (Palharim et al., 2022). The ACT removal was reduced by only 14.7 % after 4 cycle times, validating the photocatalyst stability (Fig. 8c). Both fresh and used photocatalysts were evaluated by XRD, SEM and TEM analyses, as seen in Fig. 8d-j. The XRD pattern (Fig. 8d) indicates that the material composition was practically unchanged during the photocatalytic reaction. However, four extra peaks at $2\theta = 38.1°$, 44.3°, 64.4° and 77.5°, indexed to the (111), (200), (220) and (311) planes of cubic Ag (JCPDS Card No. 00–004–0783), were observed in the used sample. This implies that some Ag^+ ions may have been reduced to Ag^0 by e^- in the conduction band and/or photo-reduced during photodegradation experiments (Qiao et al., 2015).

The SEM images of the used material (Fig. 8e-f) reveal that it remained with almost the same morphology as before its use (Fig. 2d-f). The TEM and STEM (Fig. 8g-i) images exhibit some nanorods and darker quasi-spherical particles. Both morphologies were previously observed in the fresh material (Fig. 5a-b), however, the nearly spherical particles are present in greater quantity in the spent catalyst. According to the EDS spectra (Fig. 8j), which refer to the marked regions of Fig. 8h-i, the lighter areas refer to WO_3 while the darker particles may correspond to AgCl. Finally, although the XRD pattern clearly shows the presence of Ag in the used sample (Fig. 8d), it is not possible to attribute any role to silver in terms of photocatalytic efficiency, as Ag particles were not detected in the TEM images (Figs. 5 and 8). Likewise, the LSPR effect was not observed by the DRS UV–vis analyses (Figs. S4 and S6), neither for fresh materials nor for materials after use.

Table 3 presents a list of studies that synthesized WO_3-AgCl-based photocatalysts using different technologies. It can be seen that the hydrothermal method is widely used. However, there is no consensus regarding the optimal temperature and time of synthesis, which varies from 120° to 200 °C and from 2 to 48 h, respectively, thus reinforcing the importance of a systematic study to evaluate the effect of these two conditions. Likewise, sodium tungstate, the

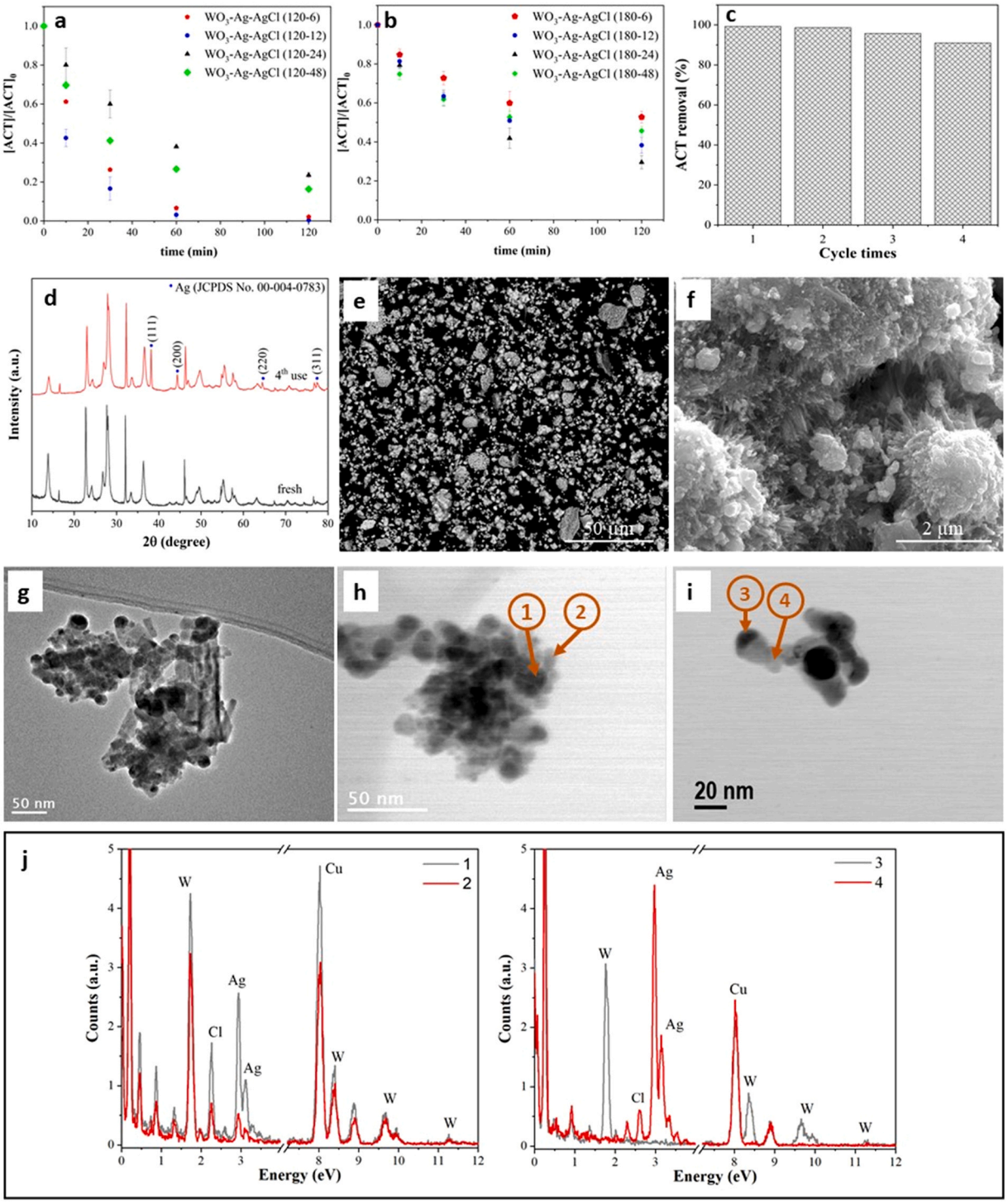

Fig. 8 – Performance of WO_3-AgCl photocatalysts in the photocatalytic degradation of acetaminophen ($[ACT]_0$ = 5.15 ± 0.25 mg L^{-1}) under simulated sunlight using (a) catalysts synthesized at 120 °C and (b) catalysts synthesized at 180 °C; (c) Reuse tests of the WO_3-AgCl (120–12) photocatalyst after 120 min; (d) XRD diffraction patterns of the fresh and reused photocatalyst; (e-f) SEM images of the used WO_3-AgCl (120–12) photocatalyst; (g) TEM images and (h-i) STEM images of the used WO_3-AgCl (120–12) photocatalyst; (j) EDS spectra.

cheapest reactant among others, is widely applied as a precursor of tungsten. Although there is unanimity for the application of an irradiation source that simulates the solar spectrum for photocatalytic assays, there are still various works that adopt dyes as model contaminants. However, the photocatalytic removal of dyes should be analyzed with caution due to the possible photosensitizing effect of the catalyst (Shaham-Waldmann and Paz, 2016). After all, regardless of the synthesis variations, all the WO_3-AgCl-based catalysts reported resulted in high photocatalytic performance, suggesting that this material is, in fact, a promising photocatalyst. Finally, our study is of great importance to understand the effects of different temperatures and synthesis times, using an easy one-step hydrothermal method with a low-cost tungsten precursor. In addition, the high photocatalytic activities obtained open perspectives for further improvements and studies on the synthesis procedure that can still be carried out.

Table 2 – ACT removal percentages and pseudo first-order kinetic constants for the WO_3-AgCl photocatalysts synthesized at different temperatures and times.

Sample[a]	ACT removal (%)[b]	k (min^{-1})[c]	R^2
WO_3-AgCl (120–6)	97.9 ± 0.2	0.044 ± 0.001	0.998
WO_3-AgCl (120–12)	99.6 ± 0.1	0.063 ± 0.006	0.941
WO_3-AgCl (120–24)	76.5 ± 1.3	0.016 ± 0.007	0.948
WO_3-AgCl (120–48)	83.6 ± 0.9	0.030 ± 0.001	0.989
WO_3-AgCl (180–6)	47.3 ± 3.1	0.011 ± 0.001	0.963
WO_3-AgCl (180–12)	61.7 ± 4.1	0.016 ± 0.001	0.984
WO_3-AgCl (180–24)	70.5 ± 3.4	0.017 ± 0.002	0.991
WO_3-AgCl (180–48)	54.3 ± 2.3	0.017 ± 0.002	0.951

[a]The first number in parentheses represents the synthesis temperature (°C) and the second number represents the synthesis time (h).
[b]After 120 min of reaction; [c]calculated in the first 30 min of reaction.

3.8. Role of oxidizing species

Reactive oxidizing species play an important role in the photodegradation of organic pollutants and are crucial for understanding the photocatalysis mechanism (Palharim et al., 2022; Hernández-Uresti et al., 2017). The main active species are known to be hydroxyl radicals ($^{\bullet}OH$), superoxide radical anions ($O_2^{\bullet-}$), holes in the valence band (h^+) and electrons in the conduction band (e^-). Thus, additional experiments were performed using tert-butanol (TBA), formic acid, 1,4-hydroquinone and potassium iodine (KI) as radical scavengers. All runs were conducted with the WO_3-AgCl (120–12) material, which showed the best photocatalytic activity using initial concentration of 0.02 mol L^{-1} for each quencher (Palharim et al., 2022; Hernández-Uresti et al., 2017). The data fitted well to the pseudo first-order kinetic and the rate constants were (Fig. 9a): 0.063 min^{-1} in the absence of radical scavengers; 0.045 min^{-1} with formic acid; 0.040 min^{-1} with TBA; 0.027 min^{-1} with KI; and 0.0001 min^{-1} with 1,4-hydroquinone. These results imply that the inhibition rate of ACT removal followed the sequence: 99.8 % with 1,4-hydroquinone > 57.1 % with KI > 37.1 % with TBA > 28.6 % with formic acid.

1,4-hydroquinone is usually used as a an $O_2^{\bullet-}$ scavenger ($k = 1.6 \times 10^7$ L mol^{-1} s^{-1}), although it can also react with $^{\bullet}OH$ radicals with a high rate constant ($k = 2.1 \times 10^{10}$ L mol^{-1} s^{-1}) at pH 6–7 (Fónagy et al., 2021). Although the pH of the solution in our experiments was ~5.0, 1,4-hydroquinone could scavenge both $O_2^{\bullet-}$ and $^{\bullet}OH$, which may be the main reactive species in the photocatalytic removal of ACT using the WO_3-AgCl (120–12) catalyst. KI, in turn, is generally used as an h^+ scavenger because iodine donates electrons to the holes in semiconductors (Schneider et al., 2020); therefore, the 57.1 %-suppression when KI was used indicates that holes are also essential in ACT removal. Considering that TBA reacts very rapidly with $^{\bullet}OH$ ($k = 4.2–7.6 \times 10^8$ L mol^{-1} s^{-1}) (Lee and Tang, 1982; Gordon et al., 1977) and its presence hindered ACT removal by 37.1 %, this radical does participate in the degradation mechanism, but it can be concluded that it is not as important as $O_2^{\bullet-}$. In turn, formic acid is widely used as an h^+ scavenger (Schneider et al., 2020; Pelaez et al., 2016); however, it can also react with $^{\bullet}OH$ with a high rate constant ($k = 1.2 \times 10^8$ L mol^{-1} s^{-1}) (Buxton et al., 1988). Thus, the reduction of rate constant by 28.6 % with the addition of formic acid indicates that competition for quenching h^+ and $^{\bullet}OH$ can occur and, as already discussed, both species take part in the removal of ACT. Nevertheless, Schneider et al. (2020). mention that, despite the low selectivity of formic acid, the mechanism is believed to happen mainly by reactions with h^+.

To better understand the radical species involved in the photocatalytic reaction, EPR experiments were performed applying DMPO as a spin-trapping agent. First, 1.5 mg of the WO_3-AgCl (120–12) catalyst and a specific amount of DMPO were added to a transparent vial containing a small magnetic stirrer. 50 mmol L^{-1} of DMPO was used for the experiments aimed at detecting $^{\bullet}OH$, while 100 mmol L^{-1} was used for $O_2^{\bullet-}$. Then, the vial was filled with water (DMPO-trapped $^{\bullet}OH$) or methanol (DMPO-trapped $O_2^{\bullet-}$) until reaching 1.5 mL. The vial was placed on a magnetic stirrer plate, 15 cm away from a high-power metal halide lamp (Fig. S7). 50 µL-samples were collected under dark conditions and after 15 min of irradiation. The samples were immediately placed in glass capillary tubes, which were later sealed with paraffine on one side. Finally, the capillary tubes were settled in an EPR quartz tube, and placed in the EPR equipment for spectrum measurement. According to Fig. 9c-d, four characteristic peaks of the DMPO-$^{\bullet}OH$ adduct and six peaks of DMPO-$O_2^{\bullet-}$ adduct can be observed; while no signal was detected under dark conditions. These results confirm the participation of both $^{\bullet}OH$ and $O_2^{\bullet-}$ species in the photocatalytic removal of ACT using the WO_3-AgCl (120–12) catalyst, corroborating the results obtained in the radical scavenging assays.

Finally, although the radical scavenging experiments nor the EPR technique do not allow us to quantify the role of each reactive species in the degradation mechanism, both analyses are essential to understand the general order of their importance. Thus, it can be said that the removal of ACT in photocatalytic experiments using the WO_3-AgCl (120–12) catalyst is driven by the following reactive species: $O_2^{\bullet-} > h^+ \sim {}^{\bullet}OH$.

3.9. Photodegradation mechanism

Photoluminescence spectroscopy (PL), a powerful method for exploring the transfer and recombination of photogenerated carriers in photocatalysts (Yuan et al., 2017), was used to provide convincing evidence for the separation of e^-/h^+ pairs. It is acknowledged that lower intensities of the emission spectra indicate that the recombination of the e^-/h^+ pairs was inhibited and consequently, greater photocatalytic activity can be achieved (Yuan et al., 2017). Fig. 9b shows the PL spectra of the bare WO_3 and the WO_3-AgCl (120–12) catalyst, at an excitation wavelength of 340 nm. Pure WO_3 presents a

Table 3 – Summary of literatures regarding WO_3-AgCl-based photocatalysts and their application for heterogeneous photocatalysis.

Photocatalyst	Synthesis method / W precursor	Irradiation source	Model contaminant / initial concentration	Maximum removal	Reference
Ag-AgCl-WO_3	Hydrothermal (200 °C, 2 h) / $Na_2WO_4{\cdot}2\,H_2O$	Solar simulator	Rhodamine B / 10 mg L^{-1}	60 % after 240 min	(Adhikari et al., 2013).
Ag-AgCl-h-WO_3	Hydrothermal for h-WO_3 (180 °C, 12 h) and precipitation + photoreduction for composite / H_2WO_4	Xenon lamp with a 420 nm cut-off filter	Rhodamine B / 15 mg L^{-1}	99.6 % after 9 min	(Chai et al., 2019).
Ag-AgCl-WO_3	Intercalation-top-chemical for WO_3 and precipitation + photoreduction for composite / H_2WO_4	Xenon lamp with a 420 nm cut-off filter	Methyl orange and rhodamine B / 20 mg L^{-1} each	~100 % after 5 min	(Chen et al., 2012).
Ag-AgCl-WO_3	Hydrothermal for WO_3 (180 °C, 9 h) and ultrasonic precipitation for composite / $Na_2WO_4{\cdot}2\,H_2O$	Xenon lamp with a 420 nm cut-off filter	4-aminobenzoic acid / 10 mg L^{-1}	90 % after 60 min	(Li et al., 2018).
Ag-AgCl-WO_3	Deposition–precipitation–photoreduction / $Na_2WO_4{\cdot}2\,H_2O$	Metal halide lamp with a 420 nm cut-off filter	4-chlorophenol / 10 mg L^{-1}	100 % after 30 min	(Ma et al., 2012).
WO_3-AgCl	Hydrothermal (120 °C, 24 h) / $Na_2WO_4{\cdot}2\,H_2O$	Solar simulator	Acetaminophen / 5 mg L^{-1}	75.4 % after 120 min	(Palharim et al., 2022).
WO_3-AgCl	Hydrothermal (160 °C, 12 h) / $Na_2WO_4{\cdot}2\,H_2O$	Xenon lamp with a 420 nm cut-off filter	Rhodamine B / 10 mg L^{-1}	100 % after 30 min	(Senthil et al., 2019).
WO_3-AgCl	Hydrothermal (180 °C, 24 h) / Ammonium tungstate	Metal halide lamp	Methyl orange and rhodamine B / 20 mg L^{-1} each	98 % for both contaminants after 75 min	(Yu et al., 2019a).
WO_3-AgCl	Hydrothermal (120 and 180 °C; 6, 12, 24 and 48 h) / $Na_2WO_4{\cdot}2\,H_2O$	Metal halide lamp	Acetaminophen / 5 mg L^{-1}	99.6 % after 120 min	This work

strong emission peak at 442 nm, as a result of the rapid recombination of the e^-/h^+ pairs. The PL peaks of the WO_3-AgCl composite decreased considerably, indicating that the separation of the e^-/h^+ pairs was increased.

Based on the previous results, a photodegradation mechanism for the WO_3-AgCl (120–12) catalyst, which showed the best photocatalytic activity, is proposed in Fig. 9e. To calculate the valence and conduction bands (VB and CB) of the semiconductors present in the composite, pure WO_3 and AgCl were synthesized following the same methodology described in Section 2.1, but without the addition of $AgNO_3$ or sodium tungstate. These materials were analyzed by UV–vis DRS and the corresponding band gap energies obtained were 2.88 eV and 3.05 for WO_3 and AgCl, respectively. The VB and CB of WO_3, calculated according to the equations described in our previous work (Palharim et al., 2022), were 3.53 and 0.65 eV, respectively; while the VB and CB of AgCl were found at 3.1 and 0.06 eV.

SEM and TEM images of the WO_3-AgCl (120–12) photocatalyst (Figs. 2d-f and 8g-i) revealed the presence of micrometric and nanometric AgCl particles, which are in close contact with agglomerated WO_3 nanorods. Aware of this, the mechanism is proposed, where AgCl and WO_3 are directly in contact. The bandgap energies of WO_3 and AgCl revealed that they cannot be highly excited by visible light (Yu et al., 2019a). However, as the irradiation source used in our experiments was a lamp that simulates the solar spectrum, the materials could be excited by the UV portion of the spectrum (Palharim et al., 2022). Thus, the photocatalytic reaction starts with the absorption of photons with energy equal to or greater than the band gap energies of WO_3 and AgCl, resulting in the generation of e^-/h^+ pairs, according to Eqs. 4–5. As the CB of AgCl is more negative than that of WO_3, electrons in the CB of AgCl will migrate to the CB of WO_3. Meanwhile, with the VB of WO_3 being more positive than the VB of AgCl, the positive holes are transferred to the VB of AgCl, and thus accumulate there. Therefore, this composite allows efficient separation of the photogenerated electrons and holes, which was confirmed by photoluminescence analysis (Fig. 9b).

$$WO_3 + h\nu \rightarrow WO_3(e^-) + WO_3(h^+) \quad (4)$$

$$AgCl + h\nu \rightarrow AgCl(e^-) + AgCl(h^+) \quad (5)$$

As the VB of AgCl is more positive than the potentials of $^{\bullet}OH/H_2O$ (2.72 eV vs. NHE) and $^{\bullet}OH/OH^-$ (2.40 eV vs. NHE), the gathered holes can react with H_2O or OH^- to generate $^{\bullet}OH$ radicals (Yuan et al., 2017). Conversely, the accumulated electrons cannot react with O_2 to form $O_2^{\bullet-}$, found to be the most important oxidative species, because the CB of WO_3 is more positive than the potential of $O_2/O_2^{\bullet-}$ (–0.33 eV vs. NHE) (Palharim et al., 2022; Yuan et al., 2017). It is worth noting, however, that the reference potentials of $O_2/O_2^{\bullet-}$, $^{\bullet}OH/H_2O$ and $^{\bullet}OH/OH^-$ are based on standard temperature and activities of the participating species, which may be different from the actual conditions; thus, it is important to consider that the experimental potentials could be slightly different from the standard potentials. The generation of $O_2^{\bullet-}$ can also be related to the occurrence of defects with intermediate energies, as indicated by the presence of low-valence tungsten ions, which were identified on the surface of the WO_3-AgCl (120–12) composite by XPS analysis (Fig. 6). In this case, W^{5+} is first photoexcited, producing extra W^{6+} and photogenerated electrons. Then, these electrons can be trapped by

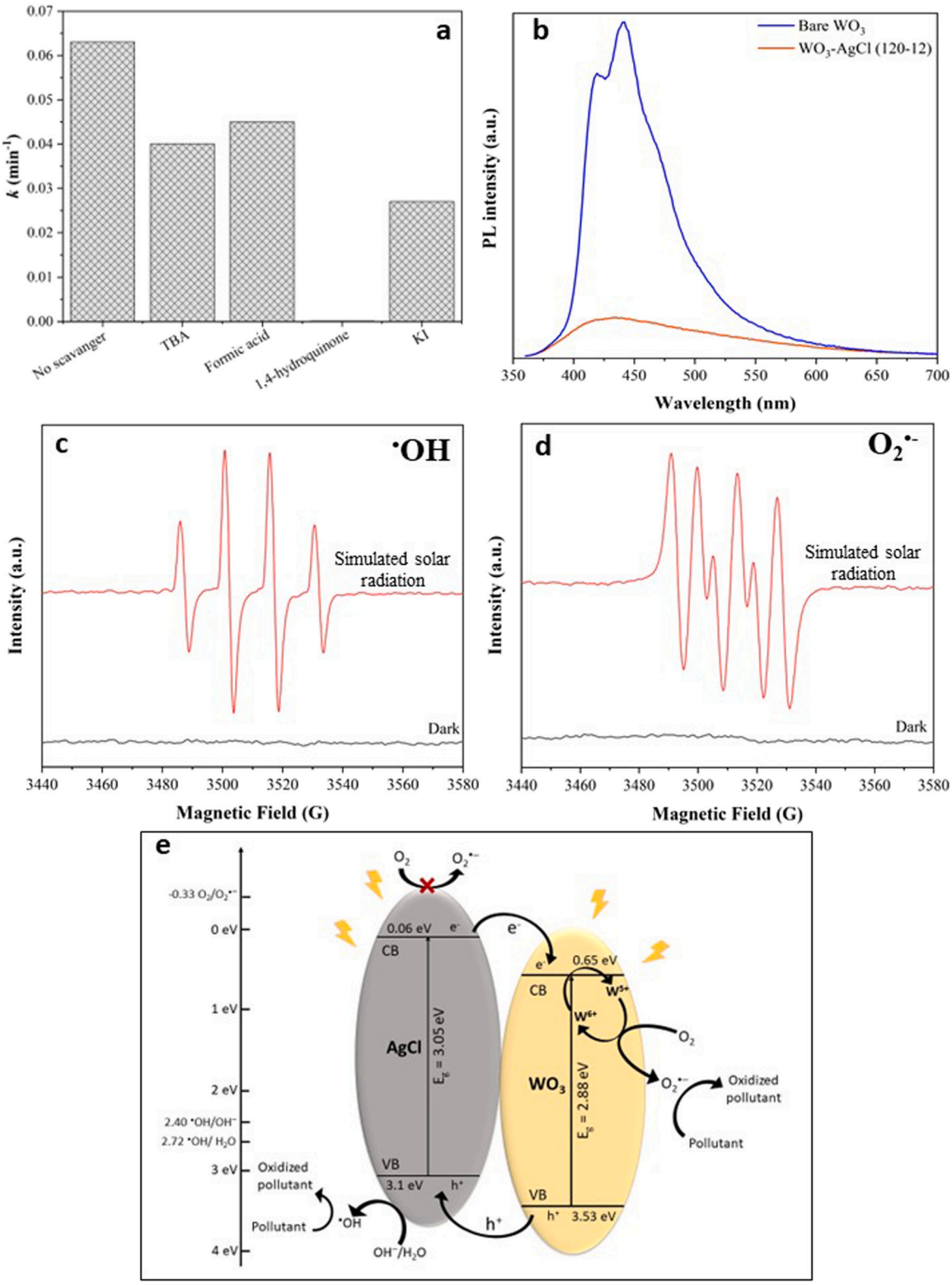

Fig. 9 – (a) Effect of different radical scavengers on the efficiency of ACT degradation using the WO_3-AgCl (120–6) catalyst. Conditions: $[ACT]_0 = 5.04 \pm 0.45\ mg\ L^{-1}$, $m_{catalyst} = 10\ mg$, $V_{solution} = 10\ mL$; dosage of scavengers = 0.02 mol L^{-1}, irradiation time = 60 min; (b) Photoluminescence spectra of pure WO_3 and WO_3-AgCl (120–12) catalyst; (c) EPR spectra of •OH radicals trapped by DMPO in aqueous medium using the WO_3-AgCl (120–6) catalyst under simulated solar radiation and of (d) $O_2^{\bullet-}$ radicals trapped by DMPO in methanol medium. Conditions: [catalyst] = 1 mg mL^{-1}, $[DMPO]_{\bullet OH} = 50\ mmol\ L^{-1}$, $[DMPO]_{O2\bullet-} = 100\ mmol\ L^{-1}$, irradiation time = 15 min; (e) Schematic diagram of the photodegradation mechanisms proposed for the WO_3-AgCl (120–12) catalyst for the degradation of ACT under simulated solar radiation.

the absorbed O_2, generating $O_2^{\bullet-}$, followed by the production of other species, such as $^{\bullet}OH$, $^{\bullet}OOH$ and $^1O_2$. Meanwhile, W^{6+} can be reduced to W^{5+} by reacting with OH^- to yield hydroxyl radicals, completing a full photocatalytic cycle (Chai et al., 2019; Li et al., 2016).

4. Conclusions

In summary, WO_3-AgCl composites were successfully synthesized by a one-step hydrothermal method, whereby the reaction temperature and time were varied. The reaction temperature of 120 °C led to the formation of rectangular prisms to quasi-spheres AgCl particles and agglomerated WO_3 nanorods; while at 180 °C, the formation of WO_3 as agglomerated rectangular prisms predominated, which were possibly completely covering the AgCl particles. As the synthesis time increased, the WO_3 nanorods became thinner at 120 °C and rectangular prisms became more agglomerated at 180 °C. AgCl growth prevailed at 120 °C and up to the first 12 h of reaction. The photocatalytic efficiency of the materials was highly influenced by the morphology of the catalysts, which was deeply affected by the temperature and extent of the synthesis reaction. The establishment of a heterojunction between AgCl and WO_3 plays an important role in photocatalytic activity, especially when the AgCl surface is not completely covered by WO_3 particles. The photocatalyst synthesized at 120 °C for 12 h showed the best photocatalytic activity, resulting in 99.6% acetaminophen (ACT) removal after 120 min of reaction, with $k = 0.063 \pm 0.006\ min^{-1}$. Stability tests revealed that the material was considerably stable after four cycles. The evaluation of oxidative species participating in the photodegradation reaction indicated that the ACT removal using the WO_3-AgCl (120–12) catalyst is driven by $O_2^{\bullet-} > h^+ \sim {}^{\bullet}OH$. Finally, these results show that the materials synthesized in the present work are an interesting option for the removal of organic contaminants using heterogeneous photocatalysis processes.

Declaration of Competing Interest

The authors declare that they have no known competing financial interests or personal relationships that could have appeared to influence the work reported in this paper.

Acknowledgments

The authors express their gratitude to the São Paulo Research Foundation (FAPESP, grant no. 2019/24158–9 and 2018/2171–6), to the Brazilian National Council for Scientific and Technological Development (CNPq, grant no.131467/2017–4) and to the Coordination for the Improvement of Higher Education Personnel – Brazil (CAPES) – Finance Code 001. Moreover, this research used facilities of the Brazilian Nanotechnology National Laboratory (LNNano), part of the Brazilian Center for Research in Energy and Materials (CNPEM), a private non-profit organization under the supervision of the Brazilian Ministry for Science, Technology, and Innovations (MCTI). The Naga Vishnu Vardhan Mogili staff is acknowledged for the assistance during the experiments (TEM-FEG-20210327).

Appendix A. Supporting information

Supplementary data associated with this article can be found in the online version at doi:10.1016/j.cherd.2022.10.045.

References

Adhikari, R., Gyawali, G., Sekino, T., Wohn Lee, S., 2013. Microwave assisted hydrothermal synthesis of Ag/AgCl/WO_3 photocatalyst and its photocatalytic activity under simulated solar light. J. Solid State Chem. 197, 560–565. https://doi.org/10.1016/j.jssc.2012.08.012

Adhikari, S., Sarkar, D., 2014. High efficient electrochromic WO_3 nanofibers. Electrochim. Acta 138, 115–123. https://doi.org/10.1016/j.electacta.2014.06.062

Bi, Q., Gao, Y., Dang, C., Wang, Z., Xue, J., 2019. Study on the photoelectrocatalytic performance of a WO_3 thin film electrode by constructing a BiOI/WO_3 heterojunction. CrystEngComm 21, 6744–6757. https://doi.org/10.1039/c9ce01183h

Biswas, S.K., Baeg, J.O., Moon, S.J., Kong, K.J., So, W.W., 2012. Morphologically different WO_3 nanocrystals in photoelectrochemical water oxidation. J. Nanopart. Res. 14, 667–679. https://doi.org/10.1007/s11051-011-0667-6

Buxton, G.V., Greenstock, C.L., Helman, W.P., Ross, A.B., 1988. Critical review of rate constants for reactions of hydrated electrons, hydrogen atoms and hydroxyl radicals ($^{\bullet}OH/^{\bullet}O^-$ in aqueous solution. J. Phys. Chem. Ref. Data 17, 513–886. https://doi.org/10.1063/1.555805

Chai, C., Liu, J., Wang, Y., Zhang, X., Duan, D., Fan, C., Wang, Y., 2019. Enhancement in photocatalytic performance of Ag–AgCl decorated with h-WO_3 and mechanism insight. Appl. Phys. A. 125, 96–106. https://doi.org/10.1007/s00339-019-2384-4

Chai, Y., Ha, F.Y., Yam, F.K., Hassan, Z., 2016. Fabrication of tungsten oxide nanostructure by sol-gel method. Procedia Chem. 19, 113–118. https://doi.org/10.1016/j.proche.2016.03.123

Chen, D., Li, T., Chen, Q., Gao, J., Fan, B., Li, J., Li, X., Zhang, R., Sun, J., Gao, L., 2012. Hierarchically plasmonic photocatalysts of Ag/AgCl nanocrystals coupled with single-crystalline WO_3 nanoplates. Nanoscale 4, 5431–5439. https://doi.org/10.1039/c2nr31030a

Chen, D., Cheng, Y., Zhou, N., Chen, P., Wang, Y., Li, K., Huo, S., Cheng, P., Peng, P., Zhang, R., Wang, L., Liu, H., Liu, Y., Ruan, R., 2020. Photocatalytic degradation of organic pollutants using TiO_2-based photocatalysts: a review. J. Clean. Prod. 268, 121725–121739. https://doi.org/10.1016/j.jclepro.2020.121725

Chen, P., Fu, H., Yang, S., Lu, K., 2022. Chemical vapor deposition-fabricated manganese-doped and potassium-doped hexagonal tungsten trioxide nanowires with enhanced gas sensing and ohotocatalytic properties. Nanomaterials 12, 1208–1221. https://doi.org/10.3390/nano12071208

Collazzo, G.C., Jahn, S.L., Carreño, N.L.V., Coletto, E.L., 2011. Temperature and reaction time effects on the structural properties of titanium dioxide nanopowders obtained via the hydrothermal method. Braz. J. Chem. Eng. 28, 265–272. https://doi.org/10.1590/S0104-66322011000200011

Costa, M.J. dos S., Costa, G. dos S., Lima, A.E.B., Júnior, G.E. da L., Longo, E., Cavalcante, L.S., Santos, R. da S., 2018. Photocurrent response and progesterone degradation by employing WO_3 films modified with platinum and silver nanoparticles. Chempluschem 83, 1153–1161. https://doi.org/10.1002/cplu.201800534

Dehdar, A., Asgari, G., Leili, M., Madrakian, T., Seid-mohammadi, A., 2021. Step-scheme BiVO4/WO3 heterojunction photocatalyst under visible LED light irradiation removing 4-chlorophenol in aqueous solutions. J. Environ. Manag. 297, 113338–113350. https://doi.org/10.1016/j.jenvman.2021.113338

Deng, S., Yang, Z., Lv, G., Zhu, Y., Li, H., Wang, F., Zhang, X., 2019. WO_3 nanosheets/g-C_3N_4 nanosheets' nanocomposite as an effective photocatalyst for degradation of rhodamine B. Appl.

Phys. A Mater. Sci. Process. 125, 44–55. https://doi.org/10.1007/s00339-018-2331-9
Fan, G., Peng, H., Zhang, J., Zheng, X., Zhu, G., Wang, S., Hong, L., 2018. Degradation of acetaminophen in aqueous solution under visible light irradiation by Bi-modified titanate nanomaterials: morphology effect, kinetics and mechanism. Catal. Sci. Technol. 8, 5906–5919. https://doi.org/10.1039/c8cy01614c
Fang, H., Cao, X., Yu, J., Lv, X., Yang, N., Wang, T., Jiang, W., 2019. Preparation of the all-solid-state Z-scheme WO_3/Ag/AgCl film on glass accelerating the photodegradation of pollutants under visible light. J. Mater. Sci. 54, 286–301. https://doi.org/10.1007/s10853-018-2856-5
Fang, W., Yang, Y., Yu, H., Dong, X., Wang, T., Wang, J., Liu, Z., Zhao, B., Yang, M., 2016. One-step synthesis of flower-shaped WO_3 nanostructures for a high-sensitivity room-temperature NOx gas sensor. RSC Adv. 6, 106880–106886. https://doi.org/10.1039/c6ra21322g
Farhadian, M., Sangpout, P., Hosseinzadeh, G., 2015. Morphology dependent photocatalytic activity of WO_3 nanostructures. J. Energy Chem. 24, 171–177. https://doi.org/10.1016/S2095-4956(15)60297-2
Fónagy, O., Szabó-Bárdos, E., Horváth, O., 2021. 1,4-Benzoquinone and 1,4-hydroquinone based determination of electron and superoxide radical formed in heterogeneous photocatalytic systems. J. Photochem. Photobiol. A Chem. 407, 113057–113071. https://doi.org/10.1016/j.jphotochem.2020.113057
Ghattavi, S., Nezamzadeh-Ejhieh, A., 2019. A brief study on the boosted photocatalytic activity of AgI/WO_3/ZnO in the degradation of methylene blue under visible light irradiation. Desalin. Water Treat. 166, 92–104. https://doi.org/10.5004/dwt.2019.24638
Gordon, S., Schmidt, K.H., Hart, E.J., 1977. A pulse radiolysis study of aqueous benzene solutions. J. Phys. Chem. 81, 104–109. https://doi.org/10.1021/j100517a003
Guerra, P., Kim, M., Shah, A., Alaee, M., Smyth, S.A., 2014. Occurrence and fate of antibiotic, analgesic/anti-inflammatory, and antifungal compounds in five wastewater treatment processes. Sci. Total Environ. 473–474, 235–243. https://doi.org/10.1016/j.scitotenv.2013.12.008
Guo, X., Deng, D., Tian, Q., 2017. One pot controllable synthesis of AgCl nanocrystals with different morphology and their photocatalytic activity. Powder Technol. 308, 206–213. https://doi.org/10.1016/j.powtec.2016.12.006
Gusmão, C.A., Palharim, P.H., Ramos, B., Teixeira, A.C.S.C., 2022. Enhancing the visible-light photoactivity of silica-supported TiO_2 for the photocatalytic treatment of pharmaceuticals in water. Environ. Sci. Pollut. Res. 29, 42215–42230. https://doi.org/10.1007/s11356-021-16718-w
Han, W., Wu, T., Wu, Q., 2021. Fabrication of WO_3/Bi_2MoO_6 heterostructures with efficient and highly selective photocatalytic degradation of tetracycline hydrochloride. J. Colloid Interface Sci. 602, 544–552. https://doi.org/10.1016/j.jcis.2021.05.128
Hassani, H., Marzbanrad, E., Zamani, C., Raissi, B., 2011. Effect of hydrothermal duration on synthesis of WO_3 nanorods. J. Mater. Sci. Mater. Electron. 22, 1264–1268. https://doi.org/10.1007/s10854-011-0297-x
Hernández-Uresti, D.B., Sanchez-Martinez, D., Torres-Martinez, L.M., 2017. Novel visible light-driven $PbMoO_4$/g-C_3N_4 hybrid composite with enhanced photocatalytic performance. J. Photochem. Photobiol. A Chem. 345, 21–26. https://doi.org/10.1016/j.jphotochem.2017.05.013
Ikehata, K., Jodeiri Naghashkar, N., Gamal El-Din, M., 2006. Degradation of aqueous pharmaceuticals by ozonation and advanced oxidation processes: a review. Ozone Sci. Eng. 28, 353–414. https://doi.org/10.1080/01919510600985937
Irfan, H., Mohamed Racik, K., Anand, S., 2018. Microstructural evaluation of $CoAl_2O_4$ nanoparticles by Williamson–Hall and size–strain plot methods. J. Asian Ceram. Soc. 6, 54–62. https://doi.org/10.1080/21870764.2018.1439606
J. Ge, Y. Zhang, Y.J. Heo, S.J. Park, Advanced design and synthesis of composite photocatalysts for the remediation of wastewater: a review, 2019. https://doi.org/10.3390/catal9020122.
Jiao, Z., Wang, J., Ke, L., Sun, X.W., Demir, H.V., 2011. Morphology-tailored synthesis of tungsten trioxide (hydrate) thin films and their photocatalytic properties. ACS Appl. Mater. Interfaces 3, 229–236. https://doi.org/10.1021/am100875z
Keller, V., Garin, F., 2003. Photocatalytic behavior of a new composite ternary system: WO_3/SiC-TiO_2. Effect of the coupling of semiconductors and oxides in photocatalytic oxidation of methylethylketone in the gas phase. Catal. Commun. 4, 377–383. https://doi.org/10.1016/S1566-7367(03)00089-X
Kleywegt, S., Payne, M., Ng, F., Fletcher, T., 2019. Environmental loadings of active pharmaceutical ingredients from manufacturing facilities in Canada. Sci. Total Environ. 646, 257–264. https://doi.org/10.1016/j.scitotenv.2018.07.240
Lee, J.H., Tang, I.N., 1982. Absolute rate constants for the hydroxyl radical reactions with ethane, furan, and thiophene at room temperature. J. Chem. Phys. 77, 4459–4463. https://doi.org/10.1063/1.444367
Li, G., Guo, C., Yan, M., Liu, S., 2016. $CsxWO_3$ nanorods: realization of full-spectrum-responsive photocatalytic activities from UV, visible to near-infrared region. Appl. Catal. B Environ. 183, 142–148. https://doi.org/10.1016/j.apcatb.2015.10.039
Li, N., Chang, T., Gao, H., Gao, X., Ge, L., 2019. Morphology-controlled WO_{3-x} homojunction: hydrothermal synthesus, adsorption properties, and visible-light-driven photocatalytic and chromic properties. Nanotechnology 30, 415601–415612. https://doi.org/10.1088/1361-6528/ab2a38
Li, P., Guo, J., Ji, X., Xiong, Y., Lai, Q., Yao, S., Zhu, Y., Zhang, Y., Xiao, P., 2021. Construction of direct Z-scheme photocatalyst by the interfacial interaction of WO_3 and SiC to enhance the redox activity of electrons and holes. Chemosphere 282, 130866–130874. https://doi.org/10.1016/j.chemosphere.2021.130866
Li, Q., Duan, G., Luo, J., Liu, X., 2018. Ultrasonic-assisted synthesis of plasmonic Z-scheme Ag/AgCl/WO_3-nanoflakes photocatalyst in geothermal water with enhanced visible-light photocatalytic performance. J. Energy Chem. 27, 826–835. https://doi.org/10.1016/j.jechem.2017.05.011
Liu, H.Y., Niu, C.G., Guo, H., Liang, C., Huang, D.W., Zhang, L., Yang, Y.Y., Li, L., 2020b. In suit constructing 2D/1D $MgIn_2S_4$/CdS heterojunction system with enhanced photocatalytic activity towards treatment of wastewater and H2 production. J. Colloid Interface Sci. 576, 264–279. https://doi.org/10.1016/j.jcis.2020.05.025
Liu, Y., Zeng, X., Easton, C.D., Li, Q., Xia, Y., Yin, Y., Hu, X., Hu, J., Xia, D., McCarthy, D.T., Deletic, A., Sun, C., Yu, J., Zhang, X., 2020a. An: In situ assembled WO_3-TiO_2 vertical heterojunction for enhanced Z-scheme photocatalytic activity. Nanoscale 12, 8775–8784. https://doi.org/10.1039/d0nr01611j
Ma, B., Guo, J., Dai, W.L., Fan, K., 2012. Ag-AgCl/WO_3 hollow sphere with flower-like structure and superior visible photocatalytic activity. Appl. Catal. B Environ. 123–124, 193–199. https://doi.org/10.1016/j.apcatb.2012.04.029
Makuła, P., Pacia, M., Macyk, W., 2018. How to correctly determine the band gap energy of modified semiconductor photocatalysts based on UV-Vis spectra. J. Phys. Chem. Lett. 9, 6814–6817. https://doi.org/10.1021/acs.jpclett.8b02892
Mestre, A.S., Carvalho, A.P., 2019. Photocatalytic degradation of pharmaceuticals carbamazepine, diclofenac, and sulfamethoxazole by semiconductor and carbon materials: a review. Molecules 24, 3702–3742. https://doi.org/10.3390/molecules24203702
Montagner, C.C., Sodré, F.F., Acayaba, R.D., Vidal, C., Campestrini, I., Locatelli, M.A., Pescara, I.C., Albuquerque, A.F., Umbuzeiro, G.A., Jardim, W.F., 2019. Ten years-snapshot of the occurrence of emerging contaminants in drinking, surface and ground waters and wastewaters from São Paulo State, Brazil. J. Braz. Chem. Soc. 30, 614–632. https://doi.org/10.21577/0103-5053.20180232
Mu, W., Xie, X., Li, X., Zhang, R., Yu, Q., Lv, K., Wei, H., Jian, Y., 2014. Characterizations of Nb-doped WO_3 nanomaterials and their enhanced photocatalytic performance. RSC Adv. 4, 36064–36070. https://doi.org/10.1039/C4RA04080E

Munawara, T., Mukhtara, F., Nadeema, M.S., Manzoorb, S., Ashiqb, M.N., Mahmoodc, K., Batoold, S., Hasand, M., Iqbal, F., 2004. Fabrication of dual Z-scheme TiO_2-WO_3-CeO_2 heterostructured nanocomposite with enhanced photocatalysis, antibacterial, and electrochemical performance. J. Alloy. Compd. 371, 162779–162794. https://doi.org/10.1016/j.jallcom.2003.10.002

Murillo-Sierra, J.C., Hernández-Ramírez, A., Hinojosa-Reyes, L., Guzmán-Mar, J.L., 2021a. A review on the development of visible light-responsive WO_3-based photocatalysts for environmental applications. Chem. Eng. J. Adv. 5, 100070–100091. https://doi.org/10.1016/j.ceja.2020.100070

Murillo-Sierra, J.C., Hernández-Ramírez, A., Zhao, Z.Y., Martínez-Hernández, A., Gracia-Pinilla, M.A., 2021b. Construction of direct Z-scheme WO_3/ZnS heterojunction to enhance the photocatalytic degradation of tetracycline antibiotic. J. Environ. Chem. Eng. 9, 105111–105124. https://doi.org/10.1016/j.jece.2021.105111

Palharim, P.H., dos, B.L.D., Fusari, R., Ramos, B., Otubo, L., Teixeira, A.C.S.C., 2022. Effect of HCl and HNO_3 on the synthesis of pure and silver-based WO_3 for improved photocatalytic activity under sunlight. J. Photochem. Photobiol. A Chem. 422, 113550–113562. https://doi.org/10.1016/j.jphotochem.2021.113550

Park, C.Y., Seo, J.M., Jo, H., Park, J., Ok, K.M., Park, T.J., 2017. Hexagonal tungsten oxide nanoflowers as enzymatic mimetics and electrocatalysts. Nature 7, 40928–40939. https://doi.org/10.1038/srep40928

Pelaez, M., Nolan, N.T., Pillai, S.C., Seery, M.K., Falaras, P., Kontos, A.G., Dunlop, P.S.M., Hamilton, J.W.J., Byrne, J.A., O'Shea, K., Entezari, M.H., Dionysiou, D.D., 2012. A review on the visible light active titanium dioxide photocatalysts for environmental applications. Appl. Catal. B Environ. 125, 331–349. https://doi.org/10.1016/j.apcatb.2012.05.036

Pelaez, M., Falaras, P., Likodimos, V., O'shea, K., de la Cruz, A.A., Dunlop, P.S.M., Byrne, J.A., Dionysiou, D.D., 2016. Use of selected scavengers for the determination of NF-TiO_2 reactive oxygen species during the degradation of microcystin- LR under visible light irradiation. J. Mol. Catal. A Chem. 15, 183–189. https://doi.org/10.1016/j.molcata.2016.09.035

Peng, H., Chen, Y., Mao, L., Zhang, X., 2017. Significant changes in the photo-reactivity of TiO_2 in the presence of a capped natural dissolved organic matter layer. Water Res. 110, 233–240. https://doi.org/10.1016/j.watres.2016.12.025

Qiao, R., Mao, M., Hu, E., Zhong, Y., Ning, J., Hu, Y., 2015. Facile formation of mesoporous $BiVO_4$/Ag/AgCl heterostructured microspheres with enhanced visible-light photoactivity. Inorg. Chem. 54, 9033–9039. https://doi.org/10.1021/acs.inorgchem.5b01303

Schneider, J.T., Firak, D.S., Ribeiro, R.R., Peralta-Zamora, P., 2020. Use of scavenger agents in heterogeneous photocatalysis: truths, half-truths, and misinterpretations. Phys. Chem. Chem. Phys. 22, 15723–15733. https://doi.org/10.1039/d0cp02411b

Senthil, R.A., Osman, S., Pan, J., Sun, M., Khan, A., Yang, V., Sun, Y., 2019. A facile single-pot synthesis of WO_3/AgCl composite with enhanced photocatalytic and photoelectrochemical performance under visible-light irradiation. Colloids Surf. A. 567, 171–183. https://doi.org/10.1016/j.colsurfa.2019.01.056

Shaham-Waldmann, N., Paz, Y., 2016. Away from TiO_2: a critical minireview on the developing of new photocatalysts for degradation of contaminants in water. Mater. Sci. Semicond. Process. 42, 72–80. https://doi.org/10.1016/j.mssp.2015.06.068

Sujiono, E.H., Zharvan, V., Poetra, S.A., Muchtar, M., Idris, A.M., Dahlan, M.Y., 2021. Structure identification of Nd_1-xYb_xFeO_3 (x = 0.01, 0.05 and 0.10) using Rietveld refinement method. Mater. Today Proc. J. 44, 3381–3384. https://doi.org/10.1016/j.matpr.2020.11.850

Taoufik, N., Boumya, W., Achak, M., Sillanpää, M., Barka, N., 2021. Comparative overview of advanced oxidation processes and biological approaches for the removal pharmaceuticals. J. Environ. Manag. 288, 112404–112426. https://doi.org/10.1016/j.jenvman.2021.112404

Thanh, N.T.K., Maclean, N., Mahiddine, S., 2014. Mechanisms of nucleation and growth of nanoparticles in solution. Chem. Rev. 114, 7610–7630. https://doi.org/10.1021/cr400544s

Tisa, F., Abdul Raman, A.A., Daud, W.M.A.Wan, 2014. Applicability of fluidized bed reactor in recalcitrant compound degradation through advanced oxidation processes: a review. J. Environ. Manag. 146, 260–275. https://doi.org/10.1016/j.jenvman.2014.07.032

Tobajas, M., Belver, C., Rodriguez, J.J., 2017. Degradation of emerging pollutants in water under solar irradiation using novel TiO_2-ZnO/clay nanoarchitectures. Chem. Eng. J. 309, 596–606. https://doi.org/10.1016/j.cej.2016.10.002

Tong, Y., Liu, Y., Dong, L., Zhao, D., Zhang, J., Lu, Y., Shen, D., Fan, X., 2006. Growth of ZnO nanostructures with different morphologies by using hydrothermal technique. J. Phys. Chem. B 110, 20263–20267. https://doi.org/10.1021/jp063312i

Vieira, Y., Pereira, H.A., Leichtweis, J., Mistura, C.M., Foletto, E.L., Oliveira, L.F.S., Dotto, G.L., 2021. Effective treatment of hospital wastewater with high-concentration diclofenac and ibuprofen using a promising technology based on degradation reaction catalyzed by Fe^0 under microwave irradiation. Sci. Total Environ. 783https://doi.org/10.1016/j.scitotenv.2021.146991. (146991–146001).

Wang, J., Khoo, E., Lee, P.S., Ma, J., 2008. Synthesis, assembly, and electrochromic properties of uniform crystalline WO_3 nanorods. J. Phys. Chem. C 112, 14306–14312. https://doi.org/10.1021/jp804035r

Wang, L., Liu, J., Wang, Y., Zhang, X., Duan, D., Fan, C., Wang, Y., 2018. Insight into the enhanced photocatalytic performance of Ag_3PO_4 modified metastable hexagonal WO_3. Colloids Surf. A Physicochem. Eng. Asp. 541, 145–153. https://doi.org/10.1016/j.colsurfa.2018.01.021

Wang, L., Hu, H., Xu, J., Zhu, S., Ding, A., Deng, C., 2019. WO_3 nanocubes: hydrothermal synthesis, growth mechanism, and photocatalytic performance. J. Mater. Res. 34, 2955–2963. https://doi.org/10.1557/jmr.2019.189

Wang, L., Zhu, Z., Wang, F., Qi, Y., Zhang, W., Wang, C., 2021a. State-of-the-art and prospects of Zn-containing layered double hydroxides (Zn-LDH)-based materials for photocatalytic water remediation. Chemosphere 278, 130367–130387. https://doi.org/10.1016/j.chemosphere.2021.130367

Wang, Q., Zhang, W., Hu, X., Xu, L., Chen, G., Li, X., 2021b. Hollow spherical WO_3/TiO_2 heterojunction for enhancing photocatalytic performance in visible-light. J. Water Process Eng. 40, 101943–101953. https://doi.org/10.1016/j.jwpe.2021.101943

Wasly, H.S., El-Sadek, M.S.A., Henini, M., 2018. Influence of reaction time and synthesis temperature on the physical properties of ZnO nanoparticles synthesized by the hydrothermal method. Appl. Phys. A. 124, 76–84. https://doi.org/10.1007/s00339-017-1482-4Influence

Yang, L., Yu, L.E., Ray, M.B., 2008. Degradation of paracetamol in aqueous solutions by TiO_2 photocatalysis. Water Res. 42, 3480–3488. https://doi.org/10.1016/j.watres.2008.04.023

You, J., Bao, W., Wang, L., Yan, A., Guo, R., 2021. Preparation, visible light-driven photocatalytic activity, and mechanism of multiphase CdS/C_3N_4 inorganic-organic hybrid heterojunction. J. Alloy. Compd. 866, 158921–158928. https://doi.org/10.1016/j.jallcom.2021.158921

Yu, C., Chen, F., Liu, Z., Yang, K., Ji, H., Li, D., Xie, W., Li, S., 2019a. Facile synthesis of a robust visible-light-driven AgCl/WO_3 composite microrod photocatalyst. J. Alloy. Compd. 809, 151844–151854. https://doi.org/10.1016/j.jallcom.2019.151844

Yuan, X., Jiang, L., Chen, X., Leng, L., Wang, H., Wu, Z., Xiong, T., Liang, J., Zeng, G., 2017. Highly efficient visible-light-induced photoactivity of Z-scheme Ag_2CO_3/Ag/WO_3 photocatalysts for

organic pollutant degradation. Environ. Sci. Nano 4, 2175–2185. https://doi.org/10.1039/C7EN00713B
Zhang, S., Chen, S., He, L., Zhang, J., Chen, G., Meng, S., Fan, Y., Zheng, X., 2020. Investigation on the mechanism and inner impetus of photogenerated charge transfer in WO_3/ZnO heterojunction photocatalysts. J. Phys. Chem. C. 124, 27916–27929. https://doi.org/10.1021/acs.jpcc.0c08860
Zhang, X., Wang, X., Meng, J., Liu, Y., Ren, M., Guo, Y., Yang, Y., 2021. Robust Z-scheme g-C_3N_4/WO_3 heterojunction photocatalysts with morphology control of WO_3 for efficient degradation of phenolic pollutants. Sep. Purif. Technol. 255, 117693–117709. https://doi.org/10.1016/j.seppur.2020.117693
Zheng, H., Ou, J.Z., Strano, M.S., Kaner, R.B., Mitchell, A., Kalantar-Zadeh, K., 2011. Nanostructured tungsten oxide – properties, synthesis, and applications. Adv. Funct. Mater. 21, 2175–2196. https://doi.org/10.1002/adfm.201002477
Zych, M., Syrek, K., Pisarek, M., Sulka, G.D., 2022. Synthesis and characterization of anodic WO_3 layers in situ doped with C, N during anodization. Electrochim. Acta 411, 140061–140071. https://doi.org/10.1016/j.electacta.2022.140061